

# 1 First Atmospheric Aerosol Monitoring Results from Geostationary 2 Environment Monitoring Spectrometer (GEMS) over Asia

3 Yeseul Cho<sup>1</sup>, Jhoon Kim<sup>1</sup>, Sujung Go<sup>2,3</sup>, Mijin Kim<sup>4</sup>, Seoyoung Lee<sup>2,3</sup>, Minseok Kim<sup>1</sup>, Heesung Chong<sup>5</sup>,  
4 Won-Jin Lee<sup>6</sup>, Dong-Won Lee<sup>6</sup>, Omar Torres<sup>3</sup>, Sang Seo Park<sup>7</sup>

5 <sup>1</sup>Department of Atmospheric Sciences, Yonsei University, Seoul, Republic of Korea

6 <sup>2</sup>Goddard Earth Sciences Technology and Research (GESTAR) II, University of Maryland, Baltimore County, Baltimore, MD  
7 21250, USA

8 <sup>3</sup>NASA Goddard Space Flight Center, Greenbelt, MD, USA

9 <sup>4</sup>Goddard Earth Sciences Technology and Research (GESTAR) II, Morgan state university, Baltimore, MD 21251, USA

10 <sup>5</sup>Center for Astrophysics | Harvard & Smithsonian, Cambridge, MA 02138, USA

11 <sup>6</sup>National Institute of Environmental Research, Incheon, Republic of Korea

12 <sup>7</sup>Department of Civil, Urban, Earth and Environmental Engineering, Ulsan National Institute of Science and Technology,  
13 Ulsan, Republic of Korea

14  
15 *Correspondence to:* Jhoon Kim ([jkim2@yonsei.ac.kr](mailto:jkim2@yonsei.ac.kr))

16 **Abstract.** Aerosol optical properties have been provided from the Geostationary Environment Monitoring Spectrometer  
17 (GEMS). ~~It is~~, the world's first geostationary earth orbit (GEO) satellite instrument designed for ~~atmospheric environmental air~~  
18 ~~quality~~ monitoring. This study describes improvements to the GEMS aerosol retrieval algorithm (AERAOD). ~~These~~, which  
19 include spectral binning, surface reflectance estimation, cloud masking, and post-processing. ~~Furthermore, the study presents,~~  
20 ~~along with~~ validation results. These enhancements are aimed at providing more accurate and reliable aerosol-~~monitoring~~  
21 results for Asia. The adoption of spectral binning in the lookup table (LUT) approach reduces random errors and enhances the  
22 stability of ~~the~~ satellite measurements. In addition, we ~~introduce~~ ~~introduced~~ a new high-resolution database for surface  
23 reflectance estimation based on the minimum reflectance method adapted to the GEMS pixel resolution. Monthly background  
24 aerosol optical depth (BAOD) values ~~are were~~ used to ~~consistently~~ estimate ~~the~~ hourly GEMS surface reflectance. ~~consistently.~~  
25 Advanced cloud-~~removal~~ techniques ~~are have been~~ implemented to significantly improve the effectiveness of cloud detection  
26 and enhance ~~the quality of~~ aerosol retrieval ~~quality~~. An innovative post-processing correction method based on machine  
27 learning is introduced to address artificial diurnal biases in aerosol optical depth (AOD) observations. ~~This~~ ~~In this~~ study  
28 ~~investigates specific, we investigated selected~~ aerosol events. ~~If~~ ~~This~~ highlights ~~the~~ capability of GEMS to monitor and provide  
29 insights into hourly aerosol optical properties during various atmospheric events. The performance of the GEMS AERAOD  
30 products ~~is was~~ validated against the Aerosol Robotic Network (AERONET) and Cloud-Aerosol Lidar with Orthogonal  
31 Polarization (CALIOP) data for the period from November 2021 to October 2022. The GEMS AOD ~~at 443 nm~~ demonstrates  
32 a strong correlation with the AERONET AOD ~~at 443 nm~~ ( $R = 0.792$ ). However, it ~~exhibits bias~~ ~~exhibited~~ ~~biased~~ patterns,  
33 including underestimation of high AOD values and overestimation ~~in of~~ low AOD conditions. Different aerosol types (highly  
34 absorbing fine, dust, and non-absorbing) ~~exhibit~~ ~~exhibited~~ distinct validation results. The GEMS single scattering albedo (SSA)  
35 ~~at 443 nm~~ retrievals ~~agree~~ ~~agreed~~ well with the AERONET ~~data~~ ~~SSA at 440 nm~~ within reasonable error ranges, with variations  
36 observed among ~~the~~ aerosol types. For GEMS AOD ~~at 443 nm~~ exceeding 0.4 (1.0), 42.76% (56.61%) and 67.25% (85.70%)  
37 of GEMS SSA data points fall within the  $\pm 0.03$  and  $\pm 0.05$  error bounds, respectively. Model-enforced post-processing  
38 correction improved the GEMS AOD and SSA ~~performance~~ ~~performance~~, thereby reducing the diurnal variation in ~~the~~ biases.  
39 The validation of the GEMS aerosol layer height (ALH) retrievals against the CALIOP data demonstrates a good agreement,  
40 with a mean bias of  $-0.225$  km, and 55.29% (71.70%) of data within  $\pm 1$  km (1.5 km).

42 **1 Introduction**

43 The regional and global monitoring of aerosol optical properties (AOPs) was conducted using satellite measurements. Low  
 44 earth orbit (LEO) instruments such as the Advanced Very High-Resolution Radiometer (AVHRR), Moderate Resolution  
 45 Imaging Spectroradiometer (MODIS), Multiangle Imaging Spectro Radiometer (MISR), Visible Infrared Imaging Radiometer  
 46 Suite (VIIRS), and Sea-viewing Wide Field-of-view Sensor (SeaWiFS), can provide daily aerosol properties for the global  
 47 domain (Hsu et al., 2004, 2006, 2017, 2019; Jackson et al., 2013; Jethva et al., 2007; Levy et al., 2013; Lyapustin et al., 2018; [Lee  
 48 et al., 2012](#); Martonchik et al., 2009; Remer et al., 2005). ~~While~~[Although](#) significant diurnal variations in AOPs have been  
 49 observed at daily and local scales; [\(Kassianov et al., 2013; Kuang et al., 2015\)](#), emphasizing the importance of geostationary  
 50 satellite measurements for both air quality and climate studies, the temporal ~~resolutions~~[resolution](#) of LEO satellites (typically  
 51 ~~one per day~~ [have](#)~~has~~ limitations in investigating the diurnal variation and transboundary transportation of aerosols  
 52 (Lennartson et al., 2018; Zhang et al., 2018). Geostationary earth ~~orbit~~[orbits](#) (GEO) instruments such as the Advanced Baseline  
 53 Imager (ABI), Geostationary Ocean Color Imager (GOCI), GOCI-II, Meteorological Imager (MI), and Advanced Himawari  
 54 Imager (AHI), have contributed to the operational monitoring of the continuous spatio-temporal variations in AOPs at  
 55 continental spatial scales with temporal resolutions of minutes to hours using the visible and near-infrared channel (Choi et al.,  
 56 2018; Kim et al., 2016; [Kim et al., 2014](#); Kondragunta et al., 2020; Lee et al., 2023; Yoshida et al., 2018).

57 ~~Besides~~[In addition to](#) spatial and temporal resolutions, [channel specification is](#) another critical consideration for satellite  
 58 aerosol ~~retrievals is channel specification. Every above mentioned instrument~~[retrieval. All instruments](#) except GOCI-II  
 59 ~~uses~~[used](#) only visible (Vis) and near-infrared channels. However, [the](#) near-ultraviolet (UV) spectral region uniquely leverages  
 60 ~~its~~[the](#) sensitivity to aerosol absorption. ~~Thereby, it~~[Therefore, this study](#) provides valuable insights into ~~aerosol~~[the](#) optical  
 61 properties [of aerosols](#). A ~~major~~[significant](#) advantage of near-UV measurements is that ~~the~~ surface reflectance in the near-UV  
 62 region is darker than that in the visible region. This enables the derivation of AOPs over a bright surface; [typically aerosol  
 63 source regions](#). In addition, observations in the UV region are sensitive to ~~aerosols'~~[aerosol](#) radiative absorption and aerosol  
 64 layer height (ALH) information ~~because~~. [The contribution of Rayleigh scattering to the total Top of the Atmosphere \(TOA\)  
 65 reflectance enhancement](#) is reduced below the aerosol layer owing to aerosol attenuation (Kayetha et al., 2022; Torres et al.,  
 66 2005).

67 The Ozone Monitoring Instrument (OMI) serves as an example of an LEO sensor that utilizes UV wavelengths for aerosol  
 68 retrievals. It has measured radiances in the 270–500 nm spectral range and offered global coverage at a spatial resolution of  
 69  $13 \times 24$  km at nadir since 2004 (Levelt et al., 2018). OMI employs two aerosol algorithms. The first one, OMAERO (Curier  
 70 et al., 2008), developed and maintained by the Royal Netherlands Meteorological Institute (KNMI), is a multiwavelength  
 71 algorithm that relies on spectral fitting procedures to derive aerosol properties. The other is the OMI near-UV aerosol retrieval  
 72 algorithm (OMAERUV). It focuses on retrieving key atmospheric aerosol properties, including ~~the~~ aerosol optical depth  
 73 (AOD), single scattering albedo (SSA), and absorbing aerosol index (AI) (Torres et al., 2007).

74 The OMAERUV algorithm has its heritage in the Total Ozone Mapping Spectrometer (TOMS) aerosol retrieval algorithm. It  
 75 uses reflectance measurements at 354 and 388 nm to determine ~~the~~ AOD and [single scattering albedo \(SSA\)](#) using the two-  
 76 channel inversion method (Torres et al., 2002; Torres et al., 2007). ~~The global~~[Global](#) statistics reported by Ahn et al. (2014)  
 77 indicate a correlation coefficient (R) of 0.81. However, OMAERUV ~~provides~~[provided](#) a lower R (0.63) over Central and East  
 78 Asia (Zhang et al., 2015). In addition, the Tropospheric Monitoring Instrument (TROPOMI) aerosol algorithm (TropOMAER)  
 79 was developed as an adaptation of [the](#) OMAERUV. A comparison between Aerosol Robotic Network (AERONET) and  
 80 TropOMAER AOD at 12 locations yielded an R of 0.82 and a root mean square error (RMSE) of 0.19 (Torres et al., 2020).

81 The Geostationary Environment Monitoring Spectrometer (GEMS) is the first UV-Vis hyperspectral satellite instrument in a

82 GEO. It is onboard ~~the~~ Geostationary Korea Multi-Purpose Satellite-2B (GEO-KOMPSAT-2B or GK-2B). ~~GEMS was~~,  
83 launched on February 19, 2020 (Kim et al., 2020). The objective of the GEMS mission is to monitor ~~the~~ hourly air quality in  
84 Asia ( $5^{\circ}\text{S}$ – $45^{\circ}\text{N}$ ,  $75^{\circ}$ – $145^{\circ}\text{E}$ ) with a fine spatial resolution ( $3.5 \times 7.7 \text{ km}^2$  ~~at~~in Seoul, South Korea). GEMS provides  
85 hyperspectral measurements covering 300–500 nm at ~~a~~0.2 nm spectral sampling and 0.6 nm full width at half maximum  
86 (FWHM) spectral resolution ~~of 0.6 nm. Considering~~. The GEMS retrieval domain coverage changes with time because of the  
87 ~~varying GEMS scan patterns with~~ the solar zenith angle (SZA), ~~the GEMS east–west scan profiles are between morning, noon,~~  
88 ~~and afternoon following the sunlit part of the globe to cover the full field of regard (FOR).~~ The GEMS aerosol retrieval  
89 (AERAOD) algorithm is based on ~~the~~ OMAERUV algorithm and the optimal estimation (OE) method by ~~finding~~determining  
90 the optimized values of AOD, SSA, and ALH from GEMS measurements at six wavelengths (354, 388, 412, 443, 477, and  
91 490 nm). ~~In order to overcome the challenge posed by the limited degree of freedom for signal in the GEMS wavelength range,~~  
92 ~~this~~This algorithm employs the two-channel inversion method ~~that is~~ used in the OMAERUV algorithm to retrieve ~~the~~ AOD  
93 and SSA. ~~to overcome the challenge posed by the limited degrees of freedom for signals in the GEMS wavelength range.~~  
94 Subsequently, these retrievals ~~are~~were used as ~~the~~ first ~~guesses~~estimates for the OE method (Kim et al., 2018). The six  
95 wavelengths in the UV-Vis region ~~contain~~contained information regarding ~~the~~ aerosol absorption in the UV region and the  
96 absorption bands of the oxygen dimer ( $\text{O}_2\text{-O}_2$ ) at 477 nm. ~~This~~Before the GEMS was launched, ~~this~~ method was ~~first~~ tested  
97 using ~~the~~ OMI Level 1 data and ~~was~~ used to derive key aerosol parameters, including AOD, SSA, ALH, UV, and VisAI (Jeong  
98 ~~et al., 2016~~; Kim et al., 2018; Go et al., 2020a, 2020b). Kim et al. (2018) reported that a comparison between AERONET and  
99 GEMS AOD at 26 locations in Asia yielded an R of 0.71 and ~~an~~ RMSE of 0.46. The percentage of GEMS SSA within the  
100 expected error range of the AERONET inversion data ( $\pm 0.03$ ) was denoted by 27.54%. Spectral variations ~~of~~in aerosol  
101 absorption in the UV-Vis region ~~were, as~~ investigated by Go et al. (2020a) ~~and it is~~, ~~were~~ applied to ~~the~~ GEMS aerosol  
102 algorithm. ~~to achieve improved AOPs retrieval. This adjustment accounts for the spectral dependence of aerosol absorption,~~  
103 ~~which was previously treated as independent of wavelength.~~ The GEMS AOD demonstrated a strong correlation with the  
104 AERONET AOD (R = 0.847 and RMSE = 0.285), and the percentage of GEMS SSA within the expected error of  $\pm 0.03$   
105 increased to 41.64% (Go et al., 2020a). To improve the accuracy of ~~the~~ GEMS aerosol retrieval, ~~Go et al. al. (2020b) tested~~  
106 the use of cloud mask information ~~and from MODIS IR channels to remove cirrus and sub-pixel cloud contamination, as well~~  
107 ~~as the~~ total dust confidence index ~~from MODIS IR channels was tested for synergy (Go et al., 2020b), for the classification of~~  
108 ~~aerosol type. The limitations associated with the UV-Vis regions of GEMS were overcome using the IR channels of other~~  
109 ~~satellites, leading to research on the synergistic use of hyperspectral satellite instruments and broadband meteorological~~  
110 ~~imagers.~~

111 However, ~~as~~because the testbed for the GEMS algorithm was on the LEO platform, ~~the~~a time-dependent retrieval bias ~~had~~was  
112 not ~~been~~observed previously ~~observed~~. The diurnal variations in ~~the~~ satellite-retrieved AOPs may differ from the actual diurnal  
113 variations ~~in the AOPs~~. This discrepancy can be ~~attributed to~~explained by the different patterns of bias observed over time  
114 among ~~the~~ different ~~geostationary~~GEO satellites and retrieval algorithms (Choi et al., 2018; Lennartson et al., 2018; Wei et al.,  
115 2019; Zhang et al., 2020). This diurnal bias in AOP measurements can originate from various factors, such as errors in the  
116 surface reflectance assumption used in the retrieval algorithm, calibration issues in the Level 1 data, or the presence of short  
117 light paths at noon (Ceamanos et al., 2023).

118 To address this ~~issue~~, Zhang et al. al. (2020) ~~developed~~ an empirical AOD bias-correction algorithm ~~was~~ developed. ~~This~~  
119 ~~algorithm utilizes~~that utilized the lowest AOD values observed within a 30-day period ~~days~~ in conjunction with the background  
120 AOD to obtain a smoothed bias curve for each pixel of the ABI AOD data ~~(Zhang et al., 2020).~~ This approach helps mitigate  
121 the impact of diurnal bias in satellite AOD retrievals to improve ~~the~~ accuracy by removing artifacts from the retrieval. By  
122 applying bias-~~correction~~ methods, more reliable diurnal variations in AOD can be explained. ~~Beyond~~In addition to traditional  
123 statistical methods, bias correction methods based on machine learning have ~~started to be~~also been proposed. Model-enforced

post-processing correction involves the use of a machine-learning-based model to predict errors in conventional aerosol retrievals (Lipponen et al. 2021, 2022a, 2022b). This method was trained to learn the relationship between the input parameters of the satellite measurements and the associated retrieval errors. This approach provides a practical and effective method to enhance the accuracy of aerosol retrieval without requiring extensive modifications to existing retrieval algorithms. It leverages machine-learning capabilities to improve the reliability and precision of hourly aerosol measurements obtained from GEO satellite observations.

In this paper, we report the first aerosol monitoring results on AOPs, including the AOD, SSA, and ALH, derived from GEMS operational observations using the GEMS aerosol retrieval algorithm. The remainder of this paper is organized as follows: Section 2 describes the GEMS data and the aerosol retrieval algorithm. It also highlights the algorithm updates after the GEMS in-orbit test (IOT) period. Section 3 discusses the post-process correction for near-real-time retrieval. Section 4 discusses the GEMS aerosol monitoring results for dust, biomass burning, and absorbing aerosol events over Asia. Section 5 presents an evaluation of the retrieved GEMS AOD, SSA, and ALH retrievals against AERONET and Cloud-Aerosol Lidar with Orthogonal Polarization (CALIOP) data, and directions for future work. Finally, Section 6 presents a summary and future work.

## 2 Data and GEMS aerosol algorithm

### 2.1 Data description

#### 2.1.1 GEMS normalized radiance

The National Institute of Environmental Research (NIER) of Korea provides the GEMS Level-1C (L1C) dataset in purpose of improving, which includes various auxiliary variables necessary for retrieval to improve the efficiency of the Level 2 algorithm process by combining parameters dispersed in different files into one file. In this study, the aerosol retrieval algorithm used radiances only with the quality flags of 0 (Good) or 2 (interpolated radiances), determined by the “bad\_pixel\_mask” variable. Rather than the GEMS irradiance, we used the KNMI solar reference spectrum to calculate the GEMS-normalized radiance (Dobber et al., 2008). The GEMS irradiance is within the range of -5% to -20% compared with the KNMI solar reference spectrum. Further improvements in L1 processing, to account for the spectral characteristics of the instrument, are ongoing. The KNMI solar reference spectrum is convolved with the GEMS spectral response function (Kang et al., 2020). GEMS-measured irradiances are planned to be employed when the NIER releases an improved version of the Sun L1C product is released by the National Institute of Environmental Research (NIER).

Normalized radiances are defined in the following equation:

$$N_{\lambda} = \frac{I_{\lambda}}{ESD \times E_{\lambda}} \quad (1)$$

where  $I$ ,  $E$ ,  $ESD$ , and  $\lambda$  are the GEMS radiance, KNMI solar reference spectrum, earth-sun distance correction factor, and wavelength (354, 388, 412, 443, 477, and 490 nm), respectively. Spectral radiance and irradiance were spectrally binned and averaged within  $\pm 2.2$  nm from each wavelength to enhance the measurement signals. Additionally, Earth-Sun distance correction was used to calculate the normalized radiance.

#### 2.1.2 AERONET

AERONET is a global ground-based remote-sensing network that measures aerosol optical, microphysical, and radiative



properties (Giles et al., 2019; Holben et al., 1998; Sinyuk et al., 2020). The measurement systems ~~used~~ used Cimel sun photometers to measure ~~the solar irradiances~~ irradiance at eight wavelengths ranging from 340 to 1020 nm and sky radiances at four wavelengths ranging from 440 to 1020 nm. The AERONET data provide global aerosol information, including ~~the~~ spectral AOD and inversion products, such as the SSA, aerosol size distribution, and refractive index. The uncertainties in AODs are wavelength-dependent. It is approximately 0.01 (Vis) to 0.02 (Near-UV) in direct sun measurements (Dubovik et al., 2002). The uncertainties of SSA are  $\pm 0.03$  when AOD exceeds 0.4 at 440 nm (Dubovik et al., 2002). For the evaluation of GEMS AOD and SSA data from November 2021 to October 2022, we used AERONET V3 Level ~~4.52.0~~ data for AOD and AERONET V3 Level ~~4.52.0~~ hybrid inversion data for SSA from all sites within the entire GEMS domain, ~~ensuring higher quality compared to Level 1.5. However, we used AERONET V3 Level 1.5, data for AOD, and AERONET V3 Level 1.5 hybrid inversion data for SSA for post-process correction to ensure a sufficient volume of data during the modelling and near-real-time processing.~~

### 2.1.3 CALIOP

The CALIOP instrument is a two-wavelength polarization-sensitive lidar on the ~~Cloud Aerosol Lidar~~ cloud aerosol lidar and ~~Infrared Pathfinder Satellite Observations~~ infrared pathfinder satellite observation (CALIPSO) satellite. It was launched on April 28, 2006 (Winker et al., 2009). CALIOP monitors the global vertical profiles of aerosols and clouds by measuring three signals: ~~the~~ backscatter intensity at 1064 nm and the orthogonally polarized components of the backscattered signal at 532 nm.

Quantitative scattering information from ~~the~~ CALIOP instruments was used as reference data ~~for validating~~ to validate the ALH obtained from passive sensors (Xu et al., 2017; Xu et al., 2019; Nanda et al., 2020; Park et al., 2023). We used ~~the~~ CALIPSO Lidar Level 2 Aerosol Profile V3-41 data to validate the GEMS ALH. CALIOP profiles of the extinction coefficient ( $\beta_{ext}(i)$ ) at the 532 nm channel were utilized to calculate the CALIOP ALH using the following equation:

$$Z_{aer} = \sum_{i=1}^n H(i) \left[ \frac{\beta_{ext}(i)}{\sum_{i=1}^n \beta_{ext}(i)} \right] \quad (2)$$

where  $\beta_{ext}(i)$  is the CALIOP profile of the 532 nm extinction coefficient at height  $H(i)$ , and  $n$  is the number of layers.

## 2.2 GEMS AERAOD retrieval algorithm

### 2.2.1 Aerosol optical properties retrieval algorithm for GEMS

The GEMS AERAOD algorithm produces AOD, SSA, and ALH ~~via data using~~ the OE method. ~~The preliminary~~ An early version of the GEMS AERAOD was developed using OMI L1B normalized radiance (Kim et al., 2018; Go et al., 2020a, 2020b). After the launch, the algorithm was tested using ~~the GEMS observation~~ observations during the IOT period, and several parts of the algorithm were updated. This section briefly describes the GEMS AERAOD algorithm, AERAOD L2 data, and updates, including the ~~Look-Up Table~~ lookup table (LUT), cloud-masking procedure, surface reflectance estimation, and post-processing after the IOT period. The general flow of the GEMS AERAOD retrieval algorithm is illustrated in Figure 1.

~~The~~ GEMS algorithm adopts ~~an~~ LUT approach to optimize computation efficiency. The LUT ~~is was~~ calculated assuming ~~the~~ AOPs of three aerosol types ~~by~~ using a radiative transfer model (RTM), the Vector Linearized Discrete Ordinate Radiative Transfer code (VLIDORT) (Spurr, 2006). The ~~AOPs of Highly~~ highly absorbing fine (HAF), Dust, and Non-absorbing (NA) are integrated from ~~the~~ AERONET inversion data and ~~are~~ applied for the RTM simulation. ~~The~~ details of the updated LUT are described in ~~section~~ Section 2.1.2. The preliminary algorithm used the OMI climatology Lambertian equivalent reflectance (OMLER v003) datasets as surface reflectance, ~~but~~ (Kleipool et al., 2008). ~~However,~~ for the GEMS AERAOD algorithm,

GEMS L2 surface reflectances at 354, 388, 412, 443, 477, and 490 nm were obtained by using the minimum reflectance method. The details of the surface reflectance estimation are described in Section 2.1.3.

The GEMS AERAOD provides UV and visible (Vis) AI to indicate the qualitative radiative absorptivity and particle size information, respectively (Torres et al., 2002). The GEMS UVAI and VisAI were calculated using the following equations:

$$AI = -100 \left[ \log \left( \frac{N_{\lambda_1}}{N_{\lambda_2}} \right)_{meas} - \log \left( \frac{N_{\lambda_1}(LER_{\lambda_1})}{N_{\lambda_2}(LER_{\lambda_2})} \right)_{calc} \right] \quad (3)$$

where  $N_{\lambda_1}$  and  $N_{\lambda_2}$  are the normalized radiances at the 354/388 (477/490) nm wavelength pair for UVAI and VisAI, respectively. The subscripts *meas* and *calc* represent the measured and calculated normalized radiances, respectively.

The aerosol types HAF, dust, and NA were selected using the UVAI and VisAI. The NA type was detected by a negative UVAI value. The dust and HAF types were distinguished by using the VisAI. HAF type was selected when UVAIs are positive and VISAI is negative. The dust type was selected when both AIs were positive. Sun glint and cloud masking leave only the pixels appropriate for aerosol retrieval. The glint mask was set for glint angles less than 35°. The details of the cloud-masking procedure are described in Section 2.1.4. The *a priori* states of AOD and SSA at 443 nm were obtained by two-channel inversion with neighboring wavelengths (354 and 388 nm) over both land and ocean. The assumption was that, with *a priori* states of ALH based on the climatology of CALIOP ALH. The *a priori* states of the AOD and SSA were supplied to solve the Levenberg-Marquardt equation (Rodgers, 2000). The optimal ALH was determined by fitting the normalized radiance between the measured and calculated values for the OE routine. The details of the GEMS aerosol inversion procedure are described by Kim et al. (2018).

To improve the accuracy of near real-time GEMS AOD retrieval, a model-enforced post-processing correction step was implemented using a random forest (RF) model. By combining GEMS aerosol retrieval with this post-processing correction model, more reliable and accurate near-real-time AOD estimates can be obtained.

### 2.1.2 LUT calculation

In this study, the AOPs were determined as described by Kim et al. (2018) and Go et al. (2020a). However, the dimensions of the LUT varied (as shown in Table 1) compared with, which is different from Kim et al. (2018). The nodes for the 412 nm SSA node for the NA were added. In addition, the nodes for the AOD in the LUT were extended to include the values at 5.0° and 10.0° because the previous maximum node was 3.6°. These modifications enable, enabling the retrieval of exceptionally severe aerosol events during GEMS observations. The preliminary yearly version of the GEMS AERAOD retrieval algorithm utilized the normalized radiance at six specific monochromatic wavelengths (354, 388, 412, 443, 477, and 490 nm). However, satellite measurements averaged over a specific wavelength range produce more stable values than measurements obtained at individual monochromatic wavelengths. This increased stability is attributed, owing to the averaging of random errors (i.e., instrument noise).

Consequently, a spectral-binning LUT approach was employed to reduce random errors and improve the measurement stability of the measurements. This allowed for enabled more reliable and consistent observations. Compared with to monochromatic wavelengths, the spectral binning method is computationally intensive. Therefore, the calculations were performed using the Mie theory without considering the non-sphericity of the dust. a forward RTM coupled with the Mie theory. The aerosol parameters, including the mean radii and standard deviations of the fine and coarse modes, respectively, of the aerosol bimodal number size distribution, fine mode particle fraction with respect to the total number concentration, and real part of the

refractive index, were used to generate the LUT (Kim et al., 2018).

The process of spectral binning LUT in the GEMS aerosol algorithm involves three steps: 1) A reference spectrum is generated using an RTM, which provides a spectral interval of 0.1 nm. 2) The calculated spectrum is convolved with the GEMS spectral response function and resampled to the target spectral grids with a resolution of 0.2 nm. (Kang et al., 2020). 3) The resampled spectrum is averaged at intervals of  $\pm 2.2$  nm at six central wavelengths (354, 388, 412, 443, 477, and 490 nm) and saved in the LUT. Intervals of  $\pm 2.2$  nm were selected to account for the calculation capacity and reduce the impact of random errors. During the retrieval process, the GEMS LIC normalized radiances, after being averaged at intervals of  $\pm 2.2$  nm at six central wavelengths, are compared with the calculated spectrum in the LUT. Through these steps, the spectral binning LUT aims to generate more stable retrieval results for aerosol properties.

### 2.1.3 Surface reflectance estimation

Several improvements were introduced in this study. These include an updated GEMS surface reflectance estimation method. The preliminary yearly version of the GEMS AERAOD retrieval algorithm used the OMI surface reflectance climatology data product (OMLER v003) (Kleipool et al. 2008), with a spatial resolution of  $0.5 \times 0.5^\circ$ . The limitation of the previous surface reflectance data was its, which is too coarse spatial resolution compared with that of GEMS pixels. This resulted pixel size, therefore, resulting in discontinuities in the GEMS AOPs owing to spatial resolution differences. To address this limitation, the updated GEMS surface reflectance has had a finer spatial resolution ( $0.1 \times 0.1^\circ$ ) to address this limitation. This aligns closely with the GEMS pixel resolution of the GEMS. This enhancement enables more accurate aerosol retrieval at the pixel level. The compiled hourly surface reflectance indirectly reflects the bidirectional reflectance distribution function (BRDF) effect. In addition, a new hourly surface reflectance database was generated using the minimum reflectance method based on the GEMS data. (Herman and Celarier, 1997; Hsu et al., 2004). The algorithm adopts the climatological minimum reflectance method for each pixel over a  $\pm 15$ -day window spanning a period of two years. Several tests were performed to evaluate different time windows and methods for constructing an accurate surface reflectance. These tests evaluated the effectiveness of using a  $\pm 15$ -day window as well as alternative options such as a previous 30-day window. In addition, different methods, including the minimum reflectance and second minimum reflectance approaches, were evaluated to determine the most suitable method for generating appropriate surface reflectance values (not included in this study).

The background AOD (BAOD) was considered in the retrieval algorithm. The BAOD represents the baseline level of AOD that is consistently present in a region. This was then used to derive the surface reflectance dataset. The Rayleigh scattering, gaseous absorption, and BAOD were corrected during the atmospheric correction process to create a surface reflectance dataset. Recent studies have shown that incorporating BAOD into an algorithm can reduce the uncertainty associated with satellite-based AOD remote sensing retrieval (Kim et al., 2014, 2021). Zhang et al. (2016) estimated the BAOD as the lowest fifth percentile of the AERONET AOD over a two-year period years and improved the performance of the VIIRS aerosol algorithm. It has been observed that Asia experiences relatively high BAOD values with seasonal variation. For example, at the Dhaka University site, the monthly BAOD over the past two years varied from a minimum of 0.124 in August to a maximum of 0.685 in April. Therefore, considering the seasonal variations in BAOD for atmospheric correction can help mitigate the uncertainty in satellite-derived AOD retrieval, particularly over Asia. The monthly BAODs were calculated using the following equation for each  $0.1 \times 0.1^\circ$  box from November 2020 to October 2021:

$$\tau_{grid,b,m}(lat, lon) = \sum_i W_i \tau_{b,m,i} / \sum_i W_i \quad (4)$$

where  $\tau_{grid,b,m}(lat, lon)$  is the interpolated BAOD 443 nm at  $(lat, lon)$  in month  $m$ .  $W_i$  is the inverse distance weighting

function, which is defined as  $e^{-d_i(lat,lon)/d_0}$ .  $d_i(lat,lon)$  is the distance between the AERONET site and the GEMS pixel, and  $d_0$  is a constant, respectively.  $\tau_{b,m,t}$  is the lowest fifth percentile of AERONET AOD over a two-year period years at AERONET site  $i$  in month  $m$ .

Figure S1 shows the monthly BAOD obtained based on the AERONET AOD data. Additionally, the fifth percentiles of the AERONET AOD 443 nm values at each AERONET site are plotted as circles for reference. It is evident that regions such as India exhibit a high BAOD of approximately 0.15 throughout the year, regardless of the month. However, seasonal variations in BAOD occurred over the Indo-Chinese Peninsula, Korea, and China. These areas experience heavy pollution from biomass burning during the dry season and dust events from the deserts. Both these factors contribute to increased atmospheric aerosol concentrations. These enhancements, including the use of hourly GEMS surface reflectance and the incorporation of monthly BAOD, can result in improved aerosol retrieval.

#### 2.1.4 Cloud masking procedure

The GEMS aerosol algorithm retrieved AOPs only for cloud-free pixels. Clouds exhibit spatial inhomogeneity and a higher brightness than aerosols. This study aimed to enhance the cloud-masking process in the GEMS aerosol algorithm by addressing the limitations of previous simple cloud-masking techniques. The previous method relied on a (Step 1) fixed threshold for reflectance at 412/477 nm and (Step 2) standard deviation test of reflectance at 477 nm within a  $3 \times 3$  pixel area. To improve the performance of cloud masking, an additional cloud-removal technique has been introduced in this study to improve the cloud masking performance. These tests included the following: (Step 3) a 470/477 nm normalized radiance ratio test. This involved a threshold test for the ratio of the normalized radiance values at 470 nm and 477 nm. This contrasts with the presence of clouds using the absorption bands of  $O_2-O_2$  due to the decrease in absorption of  $O_2-O_2$  at 477 nm in the presence of clouds (Kim et al., 2024) (Step 4). The difference between the hourly surface reflectance database and the calculated scene reflectivity at 412 nm: Significant differences indicate the presence of clouds (Torres et al., 2013). (Step 5) Standard deviation test of normalized radiance at 477 nm within a  $3 \times 3$  pixel area:  $\text{pixels} > f(\text{latitude})$ : The threshold for this test can vary based on the latitude, considering the regional differences in cloud characteristics. (Step 6) Standard deviation in  $3 \times 3$  pixels:  $\text{pixels} > f(\text{latitude})$  after 3-1, standard deviation in  $3 \times 3$  pixels:  $\text{pixels} > f(\text{latitude}, \text{number of cloud pixels detected method (1), (3), (4)})$ : The threshold for this test can vary based on the latitude and number of pixels detected as clouds from Steps 1 to 4) in  $3 \times 3$  pixels. A final cloud mask was applied after the aerosol retrieval. This included (6) filtering (Step 7) Filter out the high AOD values using  $\text{over the ocean} > f(\text{number of cloud pixels})$ : a threshold that is a function of the number of cloud pixels detected by methods (as clouds from steps 1), (3), (4), and (5) to 6 in an  $11 \times 11$ -pixel window (Lyapustin et al., 2021). This helps remove residual clouds over the ocean. By implementing these new methods, the proposed algorithm aims to improve the effectiveness of cloud detection and removal in GEMS pixels.

Quantitative analysis was performed to assess the impact of the improvements in each section on the retrieval results of GEMS AOD at 443 nm (Table S1). We analyzed the influence of each update factor on the AOD validation results. The validation periods were January, April, and July 2022. The statistics included R, RMSE, mean bias error (MBE), slope, y-offset, Q value indicating the percentage of AOD retrievals falling within the uncertainty envelope of 0.1 or  $\pm 30\%$  of AOD error range, and the Global Climate Observing System (GCOS) requirement is defined as the percentage of AOD retrieval falling within the uncertainty envelope of 0.03 or  $\pm 10\%$  for AOD error range. The early version of the GEMS AERAOD had an MBE of 0.36, indicating an overestimation of the GEMS AOD. When using KNMI irradiance instead of GEMS irradiance and changing to spectral binning LUT, Set1 resulted in a closer MBE of -0.074 to zero and an increased Q-value of 50.63%, approximately 30% higher than the results of the early version of GEMS AERAOD. Set 2 was the result of the analysis using the GEMS surface

reflectance instead of the OMI climatology values as the surface reflectance (Section 2.1.3). Set 2 showed a slight decrease in the R-value but an improvement in the Q-value by over 7%. Finally, introducing a new cloud removal method (Set3) increased R and decreased RMSE, leading to an increase in the Q value compared to Set2.

3 GEMS post-process correction for the near-real-time retrieval

The GEMS AOD ~~exhibited~~exhibits a diurnal bias pattern that ~~fluctuated~~fluctuates throughout the day. It formed a U-shape, with a minimum at 03:00 UTC (as will be demonstrated in Section 5.1). ~~To improve the accuracy of near real-time GEMS AOD retrieval, a~~ model-enforced post-~~process~~processing correction step was implemented using ~~a~~the random forest (RF) model proposed by Lipponen et al. (2021) ~~to improve the accuracy of near real-time GEMS AOD retrieval.~~

This concept was trained to learn the relationship between ~~the~~hourly GEMS data and AOD errors (GEMS-AERONET AOD) and to predict ~~the~~AOD errors at the target time. ~~To enable near real-time retrieval, the~~The proposed method consists of two main parts: modelling and prediction ~~to enable near-real-time retrieval.~~ In the modelling part, the input data for the RF model ~~includes~~included GEMS data (normalized radiances at six wavelengths, scattering angle, viewing zenith angle (VZA), relative azimuth angle (RAA), SZA UV and VisAI, aerosol type, AOD, and ~~a~~clear fraction (ClearFrac) (which is the ratio of clear-sky pixels to the total pixels within ~~the~~a 0.25° radius from the pixel center)). The data also include auxiliary information, such as time, land-sea mask, and elevation. The target data for training were the AOD errors~~. Each of these was, which were~~ calculated as the difference between the GEMS AOD and AERONET AOD at the corresponding single GEMS pixel where the AERONET site was located. ~~AERONET data are temporally matched within a ±10 min window of the GEMS measurement time. Data from three AERONET sites (Sorong, Jambi, and BMKG\_GAW\_PALU) with severe subpixel cloud contamination were excluded from the modeling to exclude cloud-contaminated pixels during the modelling process.~~ The predictors and target variables were collected for a time window ranging from N days to one day before the target time. After conducting several tests, N was determined to be 30 days. In the prediction part, the input variables, including the GEMS data and auxiliary information ~~in~~at the target time, were used for the ~~pretrained~~pre-trained RF model. Using these inputs, the model ~~predicted~~predicts the error in the GEMS AOD in ~~near~~-real-time. This predicted error value was then applied to the first ~~GEMS AOD retrieved~~ GEMS AOD ~~from using~~ the retrieval ~~algorithm~~algorithm. This resulted in the production of ~~the post-processed~~postprocessed GEMS AOD.

~~To investigate the performance in areas without AERONET data, we conducted a Leave-One-Site-Out Cross-Validation. This principle involves excluding data from one site and training the model using data from all other sites. The performance of the model was evaluated using data from excluded sites. The station selected for evaluation was excluded from the model-fitting process. For the period ranging from 30 days prior to the current day to 1 h before the target day, modelling was conducted, excluding data from one site. The predictive accuracy of the model was evaluated for one site on the target day. Figure S2 shows the statistical maps illustrating the results of the Leave-One-Site-Out Cross-Validation for post-process-corrected GEMS AOD for the one year from November 1, 2021, to October 31, 2022. In Northeast Asia, there was a notably high R, indicating a strong relationship in the AERONET data. However, sites closer to the equator tended to exhibit lower R values, around 0.5. The RMSE followed a similar pattern, with lower values in densely populated Northeast Asia, reflecting a better fit between the predicted and AERONET values in this region. The MBE in Northeast Asia tended to be close to zero, suggesting minimal bias in the predictions. In contrast, the Indian region shows negative MBE values, indicating an underestimation, whereas Southeast Asia shows positive values, signifying an overestimation.~~

~~A variable importance analysis for post-processing correction of the GEMS AOD was conducted (Figure S3). The GEMS AOD was the most crucial variable, emphasizing its direct influence on the correction process. The VZA and elevation are highly important. However, their significance can be attributed not only to their inherent properties but also to their role in conveying~~



AERONET location-related information. The aerosol type appeared to be less significant in the RF models. This result contrasts the notable importance of the GEMS UVAI and VisAI. This discrepancy can be attributed to the inaccurate aerosol-type classification in the GEMS aerosol algorithm.

In addition, the diurnal bias pattern in the GEMS SSA ~~also~~ exhibited fluctuations throughout the day, forming a bell shape with a minimum at 03:45 UTC. This is ~~shown~~discussed in Section 5.2. The post-processing method adopted was similar to that used for the AOD. This method was trained to determine the relationship between hourly GEMS data and SSA errors (the difference between GEMS at 443 nm and AERONET SSA at 440 nm) and to predict SSA errors for the target time. The key difference between the RF model predicting the AOD error and ~~that~~ predicting the SSA error is as follows: ~~the~~. The second model includes the GEMS SSA as an input variable, ~~and then, 19 input parameters are used to construct as well. A~~ variable importance analysis for the post-processing correction of the GEMS SSA was conducted (Figure S4). The GEMS SSA was the most critical variable in the correction process. The GEMS AOD also emerged as a highly influential variable in the RF model models for GEMS SSA post-process correction. In addition, the aerosol types appeared to have relatively low significance within the RF models for SSA correction.

Unlike AOD and SSA, the ~~postprocessing~~post-processing of ALH using an RF model is inherently limited. ~~CALIOP is predominantly used as reference data for ALH. Because by the fact that~~ CALIOP is an LEO satellite, and pixels co-located with GEMS ALH data are available only from 03:45 to 07:45 UTC. This ~~renders~~rendered it inaccessible as a reference hourly dataset covering 22:45–02:45 UTC. Unlike AERONET, the use of data from ground-based lidar is severely constrained by the limited number of observation stations and restricted geographical areas in which the lidars are deployed.

#### 4Aerosol4 Aerosol events

##### 4.1 Dust aerosol event (2022.04.08)

Figure 2 ~~present~~presents an example of hourly maps of the GEMS aerosol product, including AOD, SSA, and ALH, UVAI, and VisAI for April 8, 2022. ~~These~~Note that these results are the GEMS AOD, SSA, and SSAALH before post-processing. ~~The selected case is for the dust aerosol event over northwestern China.~~ The GEMS false RGB is shown using R (477 nm), G (412 nm), and B (354 nm) bands similar to those of the OMI false RGB method (Levelt et al., 2006).

As shown in Figure 2, ~~different~~the GEMS retrieval regionsdomain coverage changed with ~~respect to~~ time are shown as owing to the varying GEMS scan profile varies patterns with the SZA. Overall, the GEMS AOD ~~shows~~showed a significantly good agreement with the AERONET AOD measurements. It captures higher values in the Beijing–Hebei–Tianjin (BTH) region and lower values ~~over~~in South Korea and Japan. High GEMS AOD values were evident along the dust plume, attaining two reaching 2.0 at 06:45 UTC. In the case of SSA, the retrieval results demonstrated a relatively lower accuracy (notably in the BTH region) compared with AOD. In general, from 22:45 to 05:45 UTC, the SSA values displayed good concordance with both the AERONET and GEMS SSA. However, from 06:45 ~~to~~ 07:45 UTC, the SSA numbers did not match ~~over~~those for Beijing. Compared with the Beijing region, the results ~~are~~were more consistent ~~in~~for the dust plume. The SSA values remained relatively stable at approximately 0.92–0.96 over time. However, the GEMS SSA tended to have a positive bias compared with the AERONET values. This is ~~shown~~discussed in Section 5.2. The GEMS ALHs were ~3–4 km for the dust plume over the Taklamakan Desert and ~1.0 km over the Beijing region. The GEMS ALH exhibited continuous spatial and temporal patterns. The UVAI provides information regarding the radiative absorption of aerosols. It attained a maximum of four for dust plumes, thereby indicating significant aerosol absorption. However, over Beijing, the SSA was ~1. This indicated a marginal absorption owing to the different aerosol emission source. VisAI provides information on the aerosol size. In regions with a dust plume, the VisAI value was higher than that in the background areas. This indicated the presence of coarse aerosol particles.

400

#### 401 4.2 Biomass burning event (2022.03.19)

402 Figure 3 ~~illustrates~~ shows maps of the GEMS aerosol product at 06:45 UTC on March 19, 2022. ~~This~~ represents a biomass-  
403 burning event ~~over~~in mainland Southeast Asia. These results were obtained for the GEMS AOD and SSA before post-  
404 processing. ~~During the dry season in this region, highly absorbing fine~~ Fine pollution particles are prevalent ~~in this region~~  
405 ~~during the dry season~~ (Yin et al., 2019). The GEMS AOD > 1.6. This indicated ~~a~~ significant aerosol loading and enhancement  
406 during the event. The GEMS SSA ~~was~~ is approximately 0.88. This ~~indicated~~ indicates aerosol absorption during this event.  
407 The ALH ranged from 2 to 3 km within the biomass-burning plume. The GEMS ALH was not retrieved along the east-to-west  
408 straight line at ~22.5°N, which ~~are~~ is a bad ~~pixels~~ pixel in the CCD. The GEMS UVAI ~~showed~~ revealed hotspots and fine  
409 features associated with this event. Thus, it ~~captured~~ captures the aerosol absorption in the ultraviolet spectrum. ~~GEMS~~ VisAI  
410 ~~exhibited higher values than the background, did not clearly show signals from small particles caused by biomass burning,~~  
411 ~~indicating that signals from the surface were not completely removed. There may be limitations in considering aerosol size~~  
412 ~~information using GEMS VisAI (Go et al., 2020b).~~ This case study demonstrates that ~~the~~ GEMS provides valuable insights  
413 into aerosol properties during specific events such as biomass burning, and can capture temporal and spatial variations in AOD,  
414 SSA, ALH, UVAI, and VisAI.

415 Figure 3g shows a comparison of the CALIOP extinction coefficients at 532 nm, the CALIOP ALH, and the GEMS ALH over  
416 the CALIOP path (~~the~~ green line on the GEMS false RGB image in Figure 3a). Figure 3g illustrates ~~a clear~~ the precise  
417 relationship between the GEMS AOD and ~~the~~ accuracy of ~~the~~ GEMS ALH. ~~The accurate~~ Accurate retrieval of ALH requires  
418 the presence of a sufficient amount of aerosols in the atmosphere. ~~The~~ GEMS ALH closely ~~follows~~ followed the latitudinal  
419 variation in ~~the~~ CALIOP ALH. As the latitude increased from 18° to 21°, the GEMS ALH followed the CALIOP ALH and  
420 ~~showed~~ exhibited an increase in altitude. In the latitude range of 24°–28°, the GEMS AOD decreased, and the GEMS ALH  
421 exhibited scattered variations owing to weaker signals. In the scatter plot comparing CALIOP ALH and GEMS ALH (Figure  
422 3h), 39.88% of the pixels are within the expected error range of 0.5 km, and 68.10% of the pixels are within the expected error  
423 range of 1 km. As the GEMS AOD values decreased, the GEMS ALH pixels were more likely to ~~be~~ fall outside the expected  
424 error range.

425

#### 426 4.3 Absorbing aerosol event (2021.12.04, 2021.12.23)

427 Figure 4 shows an example of the GEMS AOD before and after post-processing for an absorbing aerosol case over ~~the~~ Indo-  
428 Gangatic Plane (IGP) at 04:45 UTC on December 4, 2021. ~~During the wintertime in this region, atmospheric~~ Atmospheric haze  
429 is prevalent ~~in this region during the winter~~ (Ram et al., 2012). Recent studies have shown that primary aerosols and precursors  
430 ~~for~~of secondary aerosols emitted from fossil fuel combustion and biomass burning are released into the atmosphere (Singh et  
431 al., 2021). Figure 4a shows ~~the~~ GEMS false RGB image with ~~the~~ AERONET stations represented by circles. ~~The color~~  
432 ~~indicates the~~ Colors indicate AERONET AOD. Two distinct aerosol plumes ~~are~~ were observed. The northwest ~~shows~~ showed an  
433 AOD of ~~~~~approximately 0.8, whereas the southeast ~~has~~ showed a value of ~~~~~approximately 1.3. Figure 4b shows the GEMS  
434 AOD data. The spatial distribution of ~~the~~ GEMS AOD ~~is~~ was similar to that of ~~the~~ AERONET AOD, ~~as shown~~ in Figure 4a.  
435 However, the values ~~are~~ were marginally lower than those of the AERONET AOD. ~~Meanwhile~~ However, the ~~post-processed~~  
436 AOD ~~increased after post-processing~~ showed an elevated value, particularly in the moderate ~~original~~ AOD range (~0.7-  
437 ~~Moreover,~~ bringing the GEMS AOD ~~was~~ closer to the AERONET AOD (Figure 4c). Specifically, at the Gandhi ~~College~~  
438 site (25.871°N, 84.128°E) and Lahore (31.480°N, 74.264°E), ~~postprocessing~~ post-processing resulted in more reasonable  
439 values.

719 Figure 5 shows the maps of the GEMS SSA and the GEMS SSA after post-processing for an absorbing aerosol case over India,  
720 Bangladesh, and mainland Southeast Asia at 03:45 UTC on December 23, 2021. ~~Figure 5a shows the~~ The GEMS false-color  
721 RGB ~~image~~-with AERONET stations, represented by circles, ~~is shown in Figure 5a~~. The color indicates the AERONET SSA  
722 at 440 nm. ~~The~~ AERONET SSA values are  $\sim 0.9$  in India and Bangladesh, and  $\sim 0.93$  in Thailand. Before ~~postprocessing~~  
723 ~~processing~~, the GEMS SSAs ~~exhibit~~ exhibited values of  $\sim 0.96$  in the Indian region and  $\sim 1.0$  in ~~the~~ other areas. However,  
724 ~~following postprocessing~~ after ~~post-processing~~, the GEMS SSA values converged ~~to be and became~~ more similar to the  
725 AERONET SSA values. Nonetheless, a marginal tendency ~~for toward~~ overestimation remained.

## 726

### 727 5 Validation in GEMS AERAOD product

728 This section evaluates the GEMS AOD and SSA at 443 nm according to ~~the~~ aerosol type and measurement time using ~~the~~  
729 AERONET data in the entire GEMS domain. We used AERONET version 3 level ~~1-52.0~~ data to validate both ~~the~~ AOD and  
730 SSA ~~to ensure a larger dataset for validation purposes, as it is quality-assured~~. Figure 6 illustrates a map of the AERONET  
731 sites used for GEMS AOD and SSA validation, in conjunction with site-specific data counts. The AERONET AOD data  
732 generally showed higher counts ~~for in~~ South Korea, ~~China~~, and Taiwan. ~~Meanwhile, sites~~ Sites in South and Southeast Asia  
733 typically ~~had have~~ fewer data points. ~~Similarly, the~~ The number of AERONET SSA data points showed a distribution similar to  
734 that of ~~the~~ AOD. ~~However, AERONET sites #38, #39, and #47 in India had over 400 validation points~~. In addition, we retrieved  
735 the GEMS ALH and compared it with the CALIPSO level 2 extinction coefficient profiles at 532 nm, as well as with the  
736 CALIOP ALH defined by Equation (2).

### 737

#### 738 5.1 Aerosol optical depth

739 In this section, the GEMS AOD at 443 nm ~~is was~~ validated against AERONET data across the entire GEMS domain from  
740 November 1, 2021, to October 31, 2022. The GEMS AOD data were spatially collocated within a  $0.25^\circ$  radius of the  
741 AERONET stations and temporally within a ~~30-min~~ minute window of the GEMS measurement time. When a specific aerosol  
742 type in the GEMS was present in more than 90% of the pixels within the validation radius, ~~an aerosol-~~ type validation was  
743 conducted.

744 Figure 7 presents the results for all the pixels and each aerosol type (HAF, dust, and NA). ~~The statistics include R, RMSE,~~  
745 ~~mean bias error (MBE), slope, y offset, Q value indicating the percentage of data points within the maximum (0.1 or 30%~~  
746 ~~AOD) error range, and the Global Climate Observing System (GCOS) requirement (defined as the maximum (0.03 or 10%~~  
747 ~~AOD)).~~ The total GEMS AOD demonstrated a good correlation with the AERONET AOD, with ~~an R of~~  $R = 0.781$ ,  $RMSE =$   
748  $0.221$ , and  $MBE = 0.792$ ,  $RMSE$  of  $0.227$ , and  $MBE$  of  $0.038047$  (Figure 7a). The Q value was calculated ~~to be~~  $54.84\%$   
749  $52.93\%$ , with  $18.3917\%$  of the AOD satisfying the GCOS requirements. However, the slope and y-intercept ~~were~~  $0.589572$   
750 and  $0.493202$ , respectively. This indicated an overestimation ~~for a of~~ low AERONET AOD and an underestimation ~~for a of~~ high  
751 AERONET AOD. ~~In the case of a low AERONET AOD, there~~ There is evidence of cloud contamination effects. ~~These result~~  
752 ~~in the case of low AERONET AOD. This results~~ in an overestimation of the retrieved GEMS AOD.

753 The validation ~~shows the~~ showed differences ~~by~~ according to aerosol type. The HAF type showed the highest R and Q values  
754 compared with the other aerosol types (Figure 7b). Pixels that deviated beyond the error range owing to ~~the~~ GEMS AOD  
755 underestimation were notably observed in two main categories: sites in the Indian region (which still showed bias  
756 notwithstanding the consideration of BAOD) and sites located in Beijing with an AERONET AOD of approximately 2.0, and  
757 a GEMS AOD of approximately 1.0. Among the three aerosol types, the dust type had the fewest samples, accounting for  $1 /$   
758  $4015$  of the NA (Figure 7c). The R-value was  $0.786821$ , and the slope was the highest among the three types. Pixels that  
759 deviated beyond the error range ~~owing due~~ to GEMS AOD underestimation were primarily observed in the Indian region. In

760 contrast, pixels exceeding the error range owing to GEMS AOD overestimation were located in Northeast Asia. Currently, ~~the~~  
761 GEMS uses the same aerosol model (number-size distribution parameters and ~~real~~ refractive index) over the entire domain for  
762 each aerosol type. However, given the varying bias patterns observed in the dust ~~typetypes~~, it is necessary to consider regional  
763 variations in the GEMS aerosol model (and, thus, the LUT) in future studies. ~~The~~ NA-type was selected most frequently among  
764 the three aerosol types (Figure 7d). Figure 7d shows that a significant number of pixels ~~arewere~~ influenced by cloud  
765 contamination, which ~~iswas~~ particularly evident in regions with low NA AOD values. ~~It appears that the~~ The GEMS aerosol  
766 cloud masking process requires further improvement, particularly over the ocean. The current cloud-masking process may not  
767 effectively distinguish small clouds (i.e., broken clouds) near ~~the~~ equatorial regions. This ~~resultsresulted~~ in an overestimation  
768 of the AOD owing to cloud contamination. This phenomenon has ~~frequently~~ been observed ~~frequently~~ at AERONET stations  
769 located near the equator. The underestimation of high AOD values ~~inby~~ the GEMS aerosol algorithm can be attributed to the  
770 ~~effecteffects~~ of the current aerosol model ~~assumptionassumptions~~ used in the algorithm. This emphasizes the importance of  
771 understanding ~~the~~ AOPs to better characterize ~~thesethem~~ in the atmosphere, particularly in the UV region.

772  
773 Figure S2S5 and Table 2 present the hourly AOD validation results and statistical metrics, including N, R, slope, y-intercept,  
774 RMSE, MBE, Q value, and GCOS. It is important to note that the ~~GEMS varies its E-E-W scan profile of the GEMS varied~~  
775 depending on the SZA. Therefore, the sites used for ~~the~~ validation may not have remained consistent over time. For example,  
776 the AERONET stations around 22:45 UTC and 23:45 UTC were ~~mostlymainly~~ used for validation in the eastern region of  
777 GEMS, whereas those around 06:45 UTC and 07:45 UTC were expected to be ~~located~~ in the western region of GEMS. A  
778 systematic error analysis ~~iswill be~~ planned in a future ~~studystudies~~. Nevertheless, the hourly validation results of the GEMS  
779 AOD provide significant insights. The hourly slopes of the GEMS AOD exhibited a ~~diurnal variationvariations~~, starting at  
780 ~~0.730725~~ at 22:45 UTC, decreasing to ~~0.534490~~ and ~~0.555 by 533~~ at 1:45 UTC and 2:45 UTC, respectively, and  
781 subsequently increasing to ~~0.647606~~ and ~~0.617632~~ at 06:45 and 7:45 UTC, respectively. However, the R-values remained  
782 relatively stable over time. Most time intervals exhibited R values of approximately 0.777 or higher except ~~for 22 at 00:45~~.  
783 Figure S2S5 and Table 2 show that the diurnal variation in GEMS AOD ~~diddoes~~ not precisely reflect the actual diurnal AOD  
784 variation. Thus, it is necessary to correct and produce a consistent dataset over time to investigate ~~the~~ diurnal variations in  
785 aerosol properties. A machine-learning model using RF was used to train the hourly dependent error characteristics, remove  
786 artifacts in the retrieval processes, and maintain the physical signals.

787 Figure 8a shows the comparison results for GEMS AOD after model-enforced post-processing correction with AERONET  
788 data. ~~For near real-time post-processing correction, data from the past 30 days were used for training. Therefore, these results~~  
789 ~~were evaluated over 11 months: from December 1, 2021, to October 31, 2022.~~ Figure 8a shows that all ~~the~~ statistical metrics  
790 improved. In particular, the slope was closer to one at ~~0.809857~~, and the y-intercept was closer to zero at ~~0.068049~~. Additionally,  
791 ~~the~~ R, RMSE, and MBE were ~~0.899920~~, ~~0.159135~~, and ~~-0.005001~~, respectively. The Q value and GCOS requirements ~~alsowere~~  
792 improved ~~to -79.13 by 82.17%~~ and ~~36.0837.29%~~, respectively. The bias near low AOD values of approximately zero was  
793 ~~reduced~~ significantly ~~reduced~~. Furthermore, ~~the~~ high AOD values were closer to the 1:1 line. Figure 8b shows the bias of the  
794 GEMS AODs before and after post-~~processprocessing~~ correction with respect to time for all ~~the~~ AOD pixels. After applying  
795 the model-enforced post-~~processprocessing~~ correction to the GEMS AOD data, significant improvements in bias were  
796 observed over the diurnal cycle. The original GEMS AOD exhibited an hourly-dependent bias ~~characteristic~~. It formed a U-  
797 shape, with a minimum value near noon, ~~at~~ 03:45 UTC. However, with the implementation of ~~thea~~ model-enforced post-  
798 processing correction, the diurnal bias was ~~mitigated~~ effectively ~~mitigated~~. This resulted in a bias value close to zero throughout  
799 the day and a ~~decreased~~ standard deviation. Figure 8c illustrates the diurnal variation in the bias of a ~~low~~ AOD (AERONET  
800 AOD < 0.4). The GEMS AOD (red circles) ~~exhibitedexhibits~~ a positive bias of ~0.1. It was ~~mostlymainly~~ corrected to values  
801 close to zero after ~~post-processingpostprocessing~~ (blue circles). However, ~~certaina~~ positive bias was observed at approximately



22:45 and 23:45 UTC; and 06:45 and 07:45 UTC. Figure 8d shows the diurnal variation in the bias of high AOD (AERONET AOD > 0.4). The diurnal variation in GEMS AOD (red circles) shows a clear U-shaped pattern with a maximum negative bias of approximately -0.2 at 0.3 UTC. However, after post-processing, the bias was still negative but less than -0.1, which is significantly closer to zero. By incorporating the predicted error, we ~~obtained~~ obtain an improved GEMS AOD that considers the uncertainties and biases inherent in the retrieval process. This approach helps reduce these biases, including a low AOD overestimation, high AOD underestimation, and artificial diurnal bias in near-real-time AOD retrievals. ~~The~~ reduction in artificial diurnal bias is crucial for ensuring the reliability of hourly GEMS AOD data. This ~~is because it~~ eliminates time-dependent discrepancies and provides a more representative hourly aerosol distribution. Users can now rely on corrected GEMS AOD data for various applications without ~~being influenced by diurnal variations in the original measurements.~~ Variable importance analysis for the post-processing correction of the GEMS AOD was conducted (Figure S3). GEMS AOD was the most important variable, emphasizing its direct influence on the correction process. VZA and elevation exhibited high importance ~~the influence of diurnal variations in the original measurements.~~ However, their significance can be attributed not only to their inherent properties but also to their role in conveying AERONET location-related information. Aerosol type appeared to have less significance in the RF models. This result contrasted with the notable importance of GEMS UVAI and VisAI. This discrepancy can originate from inaccurate aerosol type classification in the GEMS aerosol algorithm.

## 5.2 Single-scattering albedo

This section presents a comparison of the GEMS SSA at 443 nm with the AERONET SSA at 440 nm ~~in~~ over the entire GEMS domain. The validation period and collocation criteria for the AERONET sites were identical to those for ~~the~~ GEMS AOD. Similar to the AOD, when a particular aerosol type in the GEMS was detected ~~for~~ in over 90% of the pixels within a 0.25° radius, we performed aerosol-type validation. Figure 9 and Table 3 ~~display~~ show the validation results for all pixels and each aerosol type. ~~The statistics~~ Statistics, including N values and percentages ~~are, were~~ within the expected error ranges (0.03 and 0.05). The uncertainty of SSA is  $\pm 0.03$  when AERONET AOD 440 nm is over 0.4 (Dubovik et al., 2002). The gray dashed lines indicate an uncertainty envelope of  $\pm 0.03$  in SSA, whereas the black dashed lines indicate an uncertainty envelope of  $\pm 0.05$  in SSA. These reference lines help ~~to~~ assess the agreement between the GEMS SSA and AERONET data within a reasonable error range. ~~When aerosols are not abundant in the atmosphere, capturing~~ Capturing SSA signals from satellite observations is challenging ~~when atmospheric aerosols are not abundant.~~ Therefore, for validation, separate analyses were conducted for ~~the~~ cases where the GEMS AOD ~~was~~ > 0.4 (indicated by the red open circles) and the GEMS AOD was > 1.0 (~~as~~ indicated by the blue open circles). Notwithstanding the ~~large~~ significant uncertainties associated with the satellite measurements, the GEMS aerosol product showed ~~a~~ good overall agreement with the AERONET SSA. When GEMS AOD exceeds 0.4, the percentage of GEMS SSA within the expected error range of  $\pm 0.03$  is denoted by ~~42.76~~ 34.22%, and that within the expected error range of  $\pm 0.05$  is denoted by ~~67.25~~ 61.38%. When the aerosol signal is strong (when GEMS AOD exceeds 1.0), the percentage of GEMS SSA within the expected error of  $\pm 0.03$  ( $\pm 0.05$ ) increases to ~~56.61% (83.70)~~ 48.85% (84.48%). However, the ~~percentage~~ percentages within the expected error range and scatter plots varied depending on the aerosol type. For the HAF type, the SSAs ~~showed~~ exhibited the largest spread. This ~~indicated~~ indicates a lower accuracy. ~~It was~~ This is likely ~~to be~~ a result of an ineffective aerosol-type selection (red circles). However, when ~~the~~ AOD ~~exceeds~~ exceeded 1.0 (~~blue circles~~), ~~these tend, it tended~~ to approach the 1:1 line (~~blue circles~~). Moreover, the percentage falling within the expected error range of  $\pm 0.03$  increases significantly. For the dust type, the GEMS SSA exhibited a positive bias of approximately 0.04 compared with the AERONET SSA (red circles). Similarly, when the AOD ~~exceeds~~ exceeded 1.0, these biases ~~decreased~~ decreased, approaching the 1:1 line (blue circles). However, the systematic bias observed in the GEMS SSA for ~~the~~ dust type indicates the need to refine the assumed dust AOPs in the LUT. The NA type in ~~the~~ GEMS was observed to have a significantly ~~low~~ lower variability ~~compared with~~ than the AERONET SSA. The GEMS SSAs showed values close to one compared with the



844 AERONET data. According to Lee et al. (2010), the NA type is identified when the SSA is above 0.95. However, many NA-  
845 type pixels were observed, with AERONET SSA values below 0.95 in the NA type. This indicates potential inaccuracies in the  
846 classification of the absorbing and NA GEMS aerosol types. ~~Nevertheless~~ However, when the AOD ~~is~~ was high (blue circles),  
847 these classification errors ~~tended~~ to decrease. This ~~results~~ resulted in values closer to ~~those of~~ the AERONET SSA.

848 Figure ~~S4S6~~ and Table 4 present the hourly SSA validation results and statistic metrics, including the N and percentage  
849 within the expected error range of  $\pm 0.03$  ( $\pm 0.05$ ). The GEMS and AERONET SSA exhibited varying distributions over time.  
850 The difference between the GEMS and AERONET SSA was most significant at 03:45 UTC and 04:45 UTC, with a positive  
851 bias. This difference decreased at 22:45 and 23:45 UTC ~~or~~ and at 05:45 and 06:45 UTC (Figure ~~S4S6~~). Similar to the GEMS  
852 AOD, the GEMS SSA ~~showed~~ exhibited diurnal variations. These ~~values~~ are also reflected in the EE% values shown in Table  
853 4. At 22:45 and 23:45 UTC, the percentage within the expected error range of  $\pm 0.03$  exceeded ~~60%-64~~. However, it  
854 ~~reduced~~ decreased to less than ~~30~~ 19% at 03:45 UTC and 23% at 04:45 UTC before increasing again. Further studies are  
855 required to understand the bias and accuracy variations in the SSA and improve the retrieval results. This can also be  
856 attributed to the shorter path length in the observation geometry when the influence of ~~the~~ surface reflectance increases,  
857 similar to that in AODs.

858 Figure 10a presents the comparison results for the GEMS SSA after post-process correction and the AERONET data. ~~The~~  
859 ~~near real time post process correction utilized data from the preceding 30 days for training.~~ The validation period was from  
860 ~~December~~ November 1, 2021, to October 31, 2022. Notably, all ~~the~~ statistical metrics demonstrated improvements.  
861 Specifically, the percentage of GEMS SSA falling within the expected error range of  $\pm 0.03$  was ~~recorded at~~ 68.3354%,  
862 whereas the percentage within the range of  $\pm 0.05$  was ~~indicated at~~ 88.8695%. Furthermore, the SSA ~~values~~ exhibited a closer  
863 alignment with the 1:1 line. Figure 10b depicts the difference between the GEMS and AERONET SSA over the  
864 measurement time. Notably, the bias pattern observed in the GEMS SSA ~~exhibits~~ exhibited artifactual characteristics, thereby  
865 forming a bell-shaped curve. In particular, during the time interval from 01:45 to 05:45 UTC, the mean bias of GEMS SSA  
866 consistently surpassed the expected error range of  $\pm 0.03$ . However, the implementation of model-enforced post-  
867 ~~process~~ processing correction was demonstrated to be highly effective in mitigating this artificial diurnal bias. This correction  
868 methodology ~~resulted in a significant improvement~~ insignificantly improved the GEMS SSA values within the expected  
869 error range. ~~Thereby~~ Therefore, it enhanced the overall accuracy of the SSA retrieval. ~~Variable importance analysis for the~~  
870 ~~post processing correction of the GEMS SSA was conducted (Figure S5). The GEMS SSA was the most important variable~~  
871 ~~in the correction process. The GEMS AOD also emerged as a highly influential variable in the RF models for GEMS SSA~~  
872 ~~post process correction. Also, aerosol types appeared to have relatively lower significance within the RF models for SSA~~  
873 ~~correction.~~

874

### 875 5.3 Aerosol layer height

876 From November 1, 2021, to October 31, 2022, the GEMS and CALIOP data were co-located for comparison. In this section,  
877 ~~the~~ level-2 aerosol extinction coefficients at 532 nm ~~are~~ were used to calculate the CALIOP ALH. This is ~~shown in Equation~~  
878 ~~expressed as (2-).~~ GEMS ALH pixels within a  $0.05^\circ$  radius surrounding each CALIOP pixel were averaged and compared with  
879 the CALIOP ALHs within a time window of 1 h ~~from~~ of the GEMS observation time. ~~The validation~~ Validation was conducted  
880 when the GEMS AOD values were ~~larger~~ greater than 0.2. This ~~was~~ is because the error in ALH retrieval increased when the  
881 presence of aerosols in the atmosphere was insufficient. Figure 11a shows a histogram of the differences between the GEMS  
882 and CALIOP ALH. The total co-located number of data is 77,318, and the mean difference is -0.225 km. The median ~~of~~  
883 ~~differences is~~ difference was -0.167 km. This indicates that the histogram ~~distribution~~ of the differences follows a Gaussian  
884 distribution, although it is ~~skewed~~ marginally skewed in ~~the~~ positive direction. Figure 11b shows a comparison between ~~the~~

925 GEMS and CALIOP ALH. These were distributed predominantly at altitudes of less than 2 km. The percentage of data falling  
926 within the expected error of  $\pm 1$  km was 55.3%, and the percentage falling within the expected error of  $\pm 1.5$  km was 71.7%.  
927 The variability of the GEMS ALH was comparable to that of the CALIOP ALH.

#### 928

#### 929 5.4 Limitations of the current GEMS AOPs and future work

930 Figure S7 shows seasonal and regional variations as a function of UTC for each of the following four regions: Korea (33° N–  
931 39° N and 124° E–132° E), North China (33° N–34° N and 110° E–124° E), South China (21° N–33° N and 110° E–122° E),  
932 Indochina Peninsula (8° N–22° N and 92° E–110° E). The Indian region was excluded from the regional analysis because the  
933 observable area within the entire region of India varied significantly depending on the GEMS scan profiles. After gridding the  
934 GEMS AOPs into a  $0.1^\circ \times 0.1^\circ$  grid box, monthly averages were calculated. After monthly averaging, seasonal averages were  
935 calculated for each pixel only when all three months within a season had data available for the given pixel. Regional averages  
936 were calculated when more than 50% of the available values were within the domain. For the AOD, U-shaped or flat diurnal  
937 variations were observed in all four regions. In the case of SSA, higher values were observed during June, July, and August  
938 (JJA) in Korea, North China, and South China, which are considered to be influenced by aerosol hygroscopic growth owing  
939 to relatively high atmospheric humidity. However, the Indochina Peninsula showed the highest SSA values in SON (September,  
940 October, and November) and the lowest values in DJF (December, January, and February), which is consistent with the  
941 relatively low SSA values observed at the Chiang Mai AERONET site from 2011 to 2016 during DJF (Liang et al., 2019).  
942 However, there are limitations to the investigation of diurnal variations in ALH. The diurnal variations in the ALH were not  
943 consistent with the diurnal variations in the mixing layer height. One reason for the uncertainty in the ALH is that it is retrieved  
944 from the OE depending on the uncertainty of the *a priori* AOD, SSA, and ALH. Before post-processing, GEMS AOD and SSA  
945 exhibited diurnal bias patterns compared to the AERONET data (details in Sections 5.1 and 5.2). These uncertainties affect the  
946 uncertainty in the diurnal variation of ALH. Because the GEMS ALH cannot be post-corrected using CALIOP data (details in  
947 Section 3), we are considering post-process-corrected ALH using ground-based lidar observation networks (i.e., the Korea  
948 Aerosol Lidar Observation Network and the Asian dust and aerosol lidar observation network) in future studies. Therefore,  
949 one of the limitations of this study is that the GEMS ALH has limitations in the detailed investigation of diurnal variations in  
950 ALH.

951 Several methods can be employed to improve the results of the GEMS aerosol algorithm. First, additional satellite data could  
952 be integrated for cloud detection. Incorporating data from other satellite sensors with IR channels, such as the AMI, can provide  
953 complementary information for cloud masking. Secondly, it is necessary to consider the AOPs used in the LUT to improve the  
954 GEMS aerosol algorithm. It is essential to incorporate additional ground-based observations in the UV region, such as those  
955 from the Pandora Instrument and SKYNET. Collecting ground-based observations in the UV region and incorporating them  
956 into the LUT can enhance the algorithm's performance. Finally, regional LUTs with data from diverse regions that consider  
957 variability in AOPs based on regional characteristics are crucial.

#### 958

#### 959 6 Summary

960 In this study, we present the first atmospheric aerosol monitoring results from GEMS over Asia. Given that the GEMS  
961 AERAOD algorithm was developed using OMI as the input data before the GEMS launch, modifications were made  
962 considering the GEO observation characteristics during the IOT period. A new hourly surface reflectance database  
963 was created using the minimum reflectance method with a fine spatial resolution that aligned with the GEMS pixel resolution.  
964 In addition, monthly BAOD maps were incorporated to estimate the hourly GEMS surface reflectance. A new cloud-

removal techniques have significantly improved the effectiveness of cloud detection and enhanced the quality of aerosol retrievals retrieval. To avoid discrepancies between the observed and simulated radiance radiances that may arise due to because of the monochromatic assumption of the LUT calculation, we applied a spectral binning approach to the LUT calculation. Finally, post-process processing correction methods based on machine learning were used to remove the non-physical diurnal biases in the AOD and SSA retrieval. This reduced the biases over time and provided more reliable hourly GEMS aerosol products in near-real-time.

The GEMS aerosol product was products were investigated for three specific events: dust events over Northeast Asia, biomass burning in Southeast Asia, and the absorption of aerosols over absorbing aerosol in India. These events highlight the capability of the GEMS to monitor and provide insights into aerosol properties during various atmospheric events while also emphasizing the importance of post-processing for data accuracy and agreement with ground measurements.

The GEMS aerosol products were validated against the AERONET and CALIOP data for the entire GEMS domain for one year (from November 2021 to October 2022). The performance of the GEMS aerosol algorithm was validated to verify its applicability for in studying the distribution of AOPs across Asia. The validation results for each product are summarized below:

The GEMS AOD show showed a good correlation with the AERONET AOD ( $R = 0.792$ ). However, it exhibits certain bias specific biased patterns were observed. Notably, an the underestimation of AOD in high AERONET AOD and the overestimation of AOD in low AERONET AOD occurred owing to because of cloud contamination. Different aerosol types exhibited varying validation results: the HAF type with the highest R and Q values; the dust type with underestimation in India but overestimation in Northeast Asia; and the NA type with cloud contamination issues, particularly for low AOD. This indicated indicates the need for an improvement in of the cloud-masking process, particularly over the ocean. Certain deviations beyond the error range of the GEMS AOD were observed in India and Beijing. The underestimation of the high AOD values can be attributed to the aerosol model. Diurnal variation variations in the retrieval performance was were evident, with varying slopes and other comparison statistics throughout the day. As Because the testbed for the GEMS algorithm was on the LEO platform, the a time-dependent retrieval bias had was not been observed previously observed. Therefore, we adopted a model-enforced post-process correction and find found that this enhance enhanced GEMS AOD performance, reduce reduced the overall biases. This These corrected data ensure ensure the reliability for of various applications.

The GEMS SSA at 443 nm was validated against the AERONET SSA at 440 nm over the entire GEMS region. The GEMS SSA's agreement with the AERONET data was evaluated within a reasonable error range of  $\pm 0.03$  ( $\pm 0.05$ ). For GEMS AOD exceeding 0.4, 42.76 (67.25)% of GEMS SSA is within  $\pm 0.03$  (0.05) error. This increases to 56.61 (85.70)% for the strong aerosol signals (GEMS AOD above  $> 1.0$ ). However, the accuracy varies varied among the aerosol types. The HAF type has exhibited higher variability and lower accuracy. The dust type has had a marginal positive bias, particularly mainly when the AOD is was high. Similar to the AOD, the post-process processing correction for the GEMS SSA data yielded significant enhancements in the statistical metrics.

The GEMS and CALIOP data were then compared. The GEMS ALH was compared with the CALIOP ALH when the GEMS AOD exceeded 0.2. The results showed a mean difference of  $-0.225$  km, with 55.29% of data being within  $\pm 1$  km and 71.70% being within  $\pm 1.5$  km. The GEMS ALH exhibited variability similar to that of CALIOP ALH.

Several methods can be used to further improve the results of the GEMS aerosol algorithm. First, additional satellite data could be integrated for cloud detection. Incorporating data from other satellite sensors with IR channels such as the AMI can provide complementary information for cloud masking. Second, it is necessary to consider the AOPs used in the LUT to improve the GEMS aerosol algorithm. It is particularly important to incorporate more ground-based observations in the UV region, such as those from the Pandora Instrument and SKYNET. Collecting ground-based observations in the UV region and incorporating

1078 ~~these into LUT can enhance the performance of this algorithm. Finally, regional LUTs with data from diverse regions that~~  
1079 ~~consider the variability in AOPs based on regional characteristics are crucial.~~ Overall, ~~the~~ improvements ~~to~~in the GEMS aerosol  
1080 algorithm ~~contribute~~have contributed to advancing our understanding of aerosol properties and their effects on the environment.  
1081 ~~Thereby~~Therefore, it provides valuable information for diverse applications, including air quality monitoring, air quality data  
1082 assimilation, and health impact assessments in Asia.

1083  
1084 *Code availability.* The GEMS L2 AERAOD algorithm is not available publicly.

1085  
1086 *Data availability.* GEMS L2 AERAOD ~~was~~data were downloaded from the Environmental Satellite Center website  
1087 (<https://nesc.nier.go.kr/en/html/datasvc/index.do>).

1088  
1089 *Author Contribution.* YC, JK, SG, and MK designed the experiments. WL and DL provided support for ~~the~~ data collection.  
1090 SL, MK, HC, OT, and SP contributed to ~~the~~ algorithm development. YC wrote the manuscript with contributions from all ~~the~~  
1091 co-authors. JK reviewed and edited the manuscript. JK provided support and supervision. All ~~the~~ authors analyzed the  
1092 measurement data and prepared the manuscript.

1093  
1094 *Competing Interests.* At least one of the (co-)authors is a member of the editorial board of Atmospheric Measurement  
1095 Techniques.

1096  
1097 *Acknowledgements.* We thank all ~~the~~ principal investigators and their staff for establishing and maintaining the AERONET  
1098 sites used in this investigation. The CALIOP V3.41 data were obtained from the NASA Langley Research Center Atmospheric  
1099 Science Data Center at <https://asdc.larc.nasa.gov/project/CALIPSO>. The authors acknowledge the National Institute of  
1100 Environmental Research, Korea Aerospace Research Institute, for providing ~~the~~ satellite data, and Professor Myoung-Hwan  
1101 Ahn and his research group at Ewha Womans University for providing information regarding ~~the~~ GEMS specifications and  
1102 Level 1 data.

1103  
1104 *Financial Support.* This work was supported by a grant from the National Institute of Environment Research (NIER), funded  
1105 by the Ministry of Environment (MOE) of the Republic of Korea (NIER-~~2023-04-02-050~~2024-04-02-028). The GEMS  
1106 program is supported by the National Institute of Environmental Research (NIER), the Ministry of Environment, South Korea.  
1107 This project is supported by the Korea Ministry of Environment (MOE) as Public Technology Program based on Environmental  
1108 Policy (2017000160001).

## References

- Ahn, C., Torres, O., and Jethva, H.: Assessment of OMI near-UV aerosol optical depth over land, *J. Geophys. Res. Atmos.*, 119, 2457–2473, <https://doi.org/10.1002/2013jd020188>, 2014.
- Ceamanos, X., Six, B., Moparthy, S., Carrer, D., Georgeot, A., Gasteiger, J., Riedi, J., Attié, J.-L., Lyapustin, A., and Katsev, I.: Instantaneous aerosol and surface retrieval using satellites in geostationary orbit (iAERUS-GEO) – estimation of 15 min aerosol optical depth from MSG/SEVIRI and evaluation with reference data, *Atmos. Meas. Tech.*, 16, 2575–2599, <https://doi.org/10.5194/amt-16-2575-2023>, 2023.
- Choi, M., Kim, J., Lee, J., Kim, M., Park, Y.-J., Holben, B., Eck, T. F., Li, Z., and Song, C. H.: GOCI Yonsei aerosol retrieval version 2 products: an improved algorithm and error analysis with uncertainty estimation from 5-year validation over East Asia, *Atmos. Meas. Tech.*, 11, 385–408, <https://doi.org/10.5194/amt-11-385-2018>, 2018.
- Curier, R. L., Veefkind, J. P., Braak, R., Veihermann, B., Torres, O., and de Leeuw, G.: Retrieval of aerosol optical properties from OMI radiances using a multiwavelength algorithm: Application to western Europe. *J. Geophys. Res. Atmos.*, 113(D17), 2008.
- Dobber, M., Kleipool, Q., Dirksen, R., Levelt, P., Jaross, G., Taylor, S., Kelly, T., Flynn, L., Leppelmeier, G., and Rozemeijer, N.: Validation of Ozone Monitoring Instrument level 1b data products, *J. Geophys. Res.*, 113, <https://doi.org/10.1029/2007jd008665>, 2008.
- Dubovik, O. and King, M. D.: A flexible inversion algorithm for retrieval of aerosol optical properties from Sun and sky radiance measurements, *J. Geophys. Res.*, 105, 20673–20696, <https://doi.org/10.1029/2000JD900282>, 2000.
- Giles, D. M., Sinyuk, A., Sorokin, M. G., Schafer, J. S., Smirnov, A., Slutsker, I., Eck, T. F., Holben, B. N., Lewis, J. R., Campbell, J. R., Welton, E. J., Korokin, S. V., and Lyapustin, A. I.: Advancements in the Aerosol Robotic Network (AERONET) Version 3 database – automated near-real-time quality control algorithm with improved cloud screening for Sun photometer aerosol optical depth (AOD) measurements, *Atmos. Meas. Tech.*, 12, 169–209, <https://doi.org/10.5194/amt-12-169-2019>, 2019.
- Go, S., Kim, J., Mok, J., Irie, H., Yoon, J., Torres, O., Krotkov, N. A., Labow, G., Kim, M., Koo, J.-H., Choi, M., and Lim, H.: Ground-based retrievals of aerosol column absorption in the UV spectral region and their implications for GEMS measurements, *Remote Sens. Environ.*, 245, <https://doi.org/10.1016/j.rse.2020.111759>, 2020.
- Go, S., Kim, J., Park, S. S., Kim, M., Lim, H., Kim, J.-Y., Lee, D.-W., and Im, J.: Synergistic Use of Hyperspectral UV-Visible OMI and Broadband Meteorological Imager MODIS Data for a Merged Aerosol Product, *Remote Sens.*, 12, <https://doi.org/10.3390/rs12233987>, 2020.
- [Herman, J. R. and Celarier, E. A.: Earth surface reflectivity climatology at 340–380 nm from TOMS data, \*J. Geophys. Res.-Atmos.\*, 102, 28003–28011, 1997.](https://doi.org/10.1029/1997JD010280)
- Holben, B. N., Eck, T. F., Slutsker, I., Tanre, D., Buis, J. P., Setzer, A., Vermote, E., Reagan, J. A., Kaufman, Y., Nakajima, T., Lavenue, F., Jankowiak, I., and Smirnov, A.: AERONET – A federated instrument network and data archive for aerosol characterization, *Remote Sens. Environ.*, 66, 1–16, [https://doi.org/10.1016/S0034-4257\(98\)00031-5](https://doi.org/10.1016/S0034-4257(98)00031-5), 1998.
- Hsu, N. C., Lee, J., Sayer, A. M., Kim, W., Bettenhausen, C., and Tsay, S. C.: VIIRS Deep Blue Aerosol Products Over Land: Extending the EOS Long-Term Aerosol Data Records, *J. Geophys. Res. Atmos.*, 124, 4026–4053, <https://doi.org/10.1029/2018jd029688>, 2019.
- Hsu, N. C., Si-Chee, T., King, M. D., and Herman, J. R.: Aerosol properties over bright-reflecting source regions, *IEEE Trans.*



1186 Geosci. Remote Sens., 42, 557–569, <https://doi.org/10.1109/tgrs.2004.824067>, 2004.

1187 Hsu, N. C., Tsay, S. C., King, M. D., and Herman, J. R.: Deep Blue Retrievals of Asian Aerosol Properties During ACE-Asia,  
 1188 IEEE Trans. Geosci. Remote Sens., 44, 3180–3195, <https://doi.org/10.1109/tgrs.2006.879540>, 2006.

1189 Jackson, J. M., Liu, H., Laszlo, I., Kondragunta, S., Remer, L. A., Huang, J., and Huang, H.-C.: Suomi-NPP VIIRS aerosol  
 1190 algorithms and data products, J. Geophys. Res. Atmos., 118, 12,673–612,689, <https://doi.org/10.1002/2013jd020449>, 2013.

1191 [Jeong, U., Kim, J., Ahn, C., Torres, O., Liu, X., Bhartia, P. K., Spurr, R. J. D., Haffner, D., Chance, K., and Holben, B. N.: An  
 1192 optimal-estimation-based aerosol retrieval algorithm using OMI near-UV observations, Atmos. Chem. Phys., 16, 177–193,  
 1193 <https://doi.org/10.5194/acp-16-177-2016>, 2016.](https://doi.org/10.5194/acp-16-177-2016)

1194 Jethva, H., Satheesh, S. K., and Srinivasan, J.: Assessment of second-generation MODIS aerosol retrieval (Collection 005) at  
 1195 Kanpur, India, Geophys. Res. Lett., 34, <https://doi.org/10.1029/2007gl029647>, 2007.

1196 Kalashnikova, O. V., Garay, M. J., Martonchik, J. V., and Diner, D. J.: MISR Dark Water aerosol retrievals: operational  
 1197 algorithm sensitivity to particle non-sphericity, Atmos. Meas. Tech., 6, 2131–2154, <https://doi.org/10.5194/amt-6-2131-2013>,  
 1198 2013.

1199 Kang, M., Ahn, M.-H., Liu, X., Jeong, U., and Kim, J.: Spectral Calibration Algorithm for the Geostationary Environment  
 1200 Monitoring Spectrometer (GEMS), Remote Sens., 12, <https://doi.org/10.3390/rs12172846>, 2020.

1201 [Kassianov, E., Barnard, J., Pekour, M., Berg, L. K., Michalsky, J., Lantz, K., and Hodges, G.: Do diurnal aerosol changes affect  
 1202 daily average radiative forcing? Geophys. Res. Lett., 40, 3265–3269, 2013.](https://doi.org/10.1029/2013gl018269)

1203 [Kuang, Y., Zhao, C. S., Tao, J. C., and Ma, N.: Diurnal variations of aerosol optical properties in the North China Plain and  
 1204 their influences on the estimates of direct aerosol radiative effect, Atmos. Chem. Phys., 15, 5761–5772,  
 1205 <https://doi.org/10.5194/acp-15-5761-2015>, 2015.](https://doi.org/10.5194/acp-15-5761-2015)

1206 Kayetha, V., Torres, O., and Jethva, H.: Retrieval of UV–visible aerosol absorption using AERONET and OMI–MODIS  
 1207 synergy: spatial and temporal variability across major aerosol environments, Atmos. Meas. Tech., 15, 845–877,  
 1208 <https://doi.org/10.5194/amt-15-845-2022>, 2022.

1209 [Kim, M., Kim, J., Wong, M. S., Yoon, J., Lee, J., Wu, D., Chan, P. W., Nichol, J. E., Chung, C. Y., and Ou, M. L.: Improvement  
 1210 of aerosol optical depth retrieval over Hong Kong from a geostationary meteorological satellite using critical reflectance with  
 1211 background optical depth correction, Remote Sens. Environ., 142, 176–187, 2014.](https://doi.org/10.5194/amt-14-176-2014)

1212 [Kim, J., Jeong, U., Ahn, M.-H., Kim, J. H., Park, R. J., Lee, H., Song, C. H., Choi, Y.-S., Lee, K.-H., Yoo, J.-M., Jeong, M.-J.,  
 1213 Park, S. K., Lee, K.-M., Song, C.-K., Kim, S.-W., Kim, Y. J., Kim, S.-W., Kim, M., Go, S., Liu, X., Chance, K., Chan Miller,  
 1214 C., Al-Saadi, J., Veihelmann, B., Bhartia, P. K., Torres, O., Abad, G. G., Haffner, D. P., Ko, D. H., Lee, S. H., Woo, J.-H.,  
 1215 Chong, H., Park, S. S., Nicks, D., Choi, W. J., Moon, K.-J., Cho, A., Yoon, J., Kim, S.-k., Hong, H., Lee, K., Lee, H., Lee, S.,  
 1216 Choi, M., Veefkind, P., Levelt, P. F., Edwards, D. P., Kang, M., Eo, M., Bak, J., Baek, K., Kwon, H.-A., Yang, J., Park, J., Han,  
 1217 K. M., Kim, B.-R., Shin, H.-W., Choi, H., Lee, E., Chong, J., Cha, Y., Koo, J.-H., Irie, H., Hayashida, S., Kasai, Y., Kanaya,  
 1218 Y., Liu, C., Lin, J., Crawford, J. H., Carmichael, G. R., Newchurch, M. J., Lefer, B. L., Herman, J. R., Swap, R. J., Lau, A. K.  
 1219 H., Kurosu, T. P., Jaross, G., Ahlers, B., Dobber, M., McElroy, C. T., and Choi, Y.: New Era of Air Quality Monitoring from  
 1220 Space: Geostationary Environment Monitoring Spectrometer \(GEMS\), Bull. Am. Meteorol. Soc., 101, E1–E22,  
 1221 <https://doi.org/10.1175/bams-d-18-0013.1>, 2020.](https://doi.org/10.1029/2019gl083441)

1222 Kim, M., Kim, J., Jeong, U., Kim, W., Hong, H., Holben, B., Eck, T. F., Lim, J. H., Song, C. K., Lee, S., and Chung, C. Y.:  
 1223 Aerosol optical properties derived from the DRAGON-NE Asia campaign, and implications for a single-channel algorithm to

- 1224 retrieve aerosol optical depth in spring from Meteorological Imager (MI) on-board the Communication, Ocean, and  
1225 Meteorological Satellite (COMS), *Atmos. Chem. Phys.*, 16, 1789–1808, <https://doi.org/10.5194/acp-16-1789-2016>, 2016.
- 1226 Kim, M., Kim, J., Torres, O., Ahn, C., Kim, W., Jeong, U., Go, S., Liu, X., Moon, K., and Kim, D.-R.: Optimal Estimation-  
1227 Based Algorithm to Retrieve Aerosol Optical Properties for GEMS Measurements over Asia, *Remote Sens.*, 10,  
1228 <https://doi.org/10.3390/rs10020162>, 2018.
- 1229 Kim, M., Kim, S. H., Kim, W. V., Lee, Y. G., Kim, J., and Kafatos, M. C.: Assessment of Aerosol optical depth under  
1230 background and polluted conditions using AERONET and VIIRS datasets, *Atmos. Environ.*, 245,  
1231 <https://doi.org/10.1016/j.atmosenv.2020.117994>, 2021.
- 1232 Kleipool, Q. L., Dobber, M. R., de Haan, J. F., and Levelt, P. F.: Earth surface reflectance climatology from 3 years of OMI  
1233 data, *J. Geophys. Res.*, 113, <https://doi.org/10.1029/2008jd010290>, 2008.
- 1234 Kondragunta, S., Laszlo, I., Zhang, H., Ciren, P., and Huff, A.: Air Quality Applications of ABI Aerosol Products from the  
1235 GOES-R Series, in: *The GOES-R Series: A New Generation of Geostationary Environmental Satellites*, Elsevier, Amsterdam,  
1236 the Netherlands, Oxford, UK, Cambridge MA, USA, 203–217, 2020.
- 1237 [Lee, J., Kim, J., Yang, P., and Hsu, N. C.: Improvement of aerosol optical depth retrieval from MODIS spectral reflectance  
1238 over the global ocean using new aerosol models archived from AERONET inversion data and tri-axial ellipsoidal dust database.  
1239 \*Atmos. Chem. Phys.\*, 12, 7087–7102, <https://doi.org/10.5194/acp-12-7087-2012>, 2012.](#)
- 1240 Lee, S., Choi, M., Kim, J., Park, Y. J., Choi, J. K., Lim, H., Lee, J., Kim, M., and Cho, Y.: Retrieval of aerosol optical properties  
1241 from GOCI-II observations: Continuation of long-term geostationary aerosol monitoring over East Asia, *Sci. Total Environ.*,  
1242 903, 166504, <https://doi.org/10.1016/j.scitotenv.2023.166504>, 2023.
- 1243 Lee, Y., Ahn, M.-H., Kang, M., and Eo, M.: Spectral replacement using machine learning methods for continuous mapping of  
1244 the Geostationary Environment Monitoring Spectrometer (GEMS), *Atmos. Meas. Tech.*, 16, 153–168,  
1245 <https://doi.org/10.5194/amt-16-153-2023>, 2023.
- 1246 Lennartson, E. M., Wang, J., Gu, J., Castro Garcia, L., Ge, C., Gao, M., Choi, M., Saide, P. E., Carmichael, G. R., Kim, J., and  
1247 Janz, S. J.: Diurnal variation of aerosol optical depth and PM<sub>2.5</sub> in South Korea: a synthesis from AERONET, satellite (GOCI),  
1248 KORUS-AQ observation, and the WRF-Chem model, *Atmos. Chem. Phys.*, 18, 15125–15144, <https://doi.org/10.5194/acp-18-15125-2018>, 2018.
- 1250 Levelt, P. F., van den Oord, G. H. J., Dobber, M. R., Malkki, A., Huib, V., Johan de, V., Stammes, P., Lundell, J. O. V., and  
1251 Saari, H.: The ozone monitoring instrument, *IEEE Trans. Geosci. Remote Sens.*, 44, 1093–1101,  
1252 <https://doi.org/10.1109/tgrs.2006.872333>, 2006.
- 1253 Levelt, P. F., Joiner, J., Tamminen, J., Veefkind, J. P., Bhartia, P. K., Stein Zweers, D. C., Duncan, B. N., Streets, D. G., Eskes,  
1254 H., van der A, R., McLinden, C., Fioletov, V., Carn, S., de Laat, J., DeLand, M., Marchenko, S., McPeters, R., Ziemke, J., Fu,  
1255 D., Liu, X., Pickering, K., Apituley, A., González Abad, G., Arola, A., Boersma, F., Chan Miller, C., Chance, K., de Graaf, M.,  
1256 Hakkarainen, J., Hassinen, S., Ialongo, I., Kleipool, Q., Krotkov, N., Li, C., Lamsal, L., Newman, P., Nowlan, C., Suleiman,  
1257 R., Tilstra, L. G., Torres, O., Wang, H., and Wargan, K.: The Ozone Monitoring Instrument: overview of 14 years in space,  
1258 *Atmos. Chem. Phys.*, 18, 5699–5745, <https://doi.org/10.5194/acp-18-5699-2018>, 2018.
- 1259 Levy, R. C., Mattoo, S., Munchak, L. A., Remer, L. A., Sayer, A. M., Patadia, F., and Hsu, N. C.: The Collection 6 MODIS  
1260 aerosol products over land and ocean, *Atmos. Meas. Tech.*, 6, 2989–3034, <https://doi.org/10.5194/amt-6-2989-2013>, 2013.
- 1261 [Liang, Y., Che, H., Gui, K., Zheng, Y., Yang, X., Li, X., Liu, C., Sheng, Z., Sun, T., and Zhang, X.: Impact of Biomass Burning](#)

1262 [in South and Southeast Asia on Background Aerosol in Southwest China, \*Aerosol Air Qual. Res.\*, 19, 1188–1204,](#)  
1263 <https://doi.org/10.4209/AAQR.2018.08.0324>, 2019.

1264 Lipponen, A., Kolehmainen, V., Kolmonen, P., Kukkurainen, A., Mielonen, T., Sabater, N., Sogacheva, L., Virtanen, T. H., and  
1265 Arola, A.: Model-enforced post-process correction of satellite aerosol retrievals, *Atmos. Meas. Tech.*, 14, 2981–2992,  
1266 <https://doi.org/10.5194/amt-14-2981-2021>, 2021.

1267 Lipponen, A., Reinvall, J., Väisänen, A., Taskinen, H., Lähivaara, T., Sogacheva, L., Kolmonen, P., Lehtinen, K., Arola, A.,  
1268 and Kolehmainen, V.: Deep-learning-based post-process correction of the aerosol parameters in the high-resolution Sentinel-  
1269 3 Level-2 Synergy product, *Atmos. Meas. Tech.*, 15, 895–914, <https://doi.org/10.5194/amt-15-895-2022>, 2022.

1270 Lyapustin, A., Wang, Y., Go, S., Choi, M., Korkin, S., Huang, D., Knyazikhin, Y., Blank, K., and Marshak, A.: Atmospheric  
1271 Correction of DSCOVR EPIC: Version 2 MAIAC Algorithm, *Front. Remote Sens.*, 2,  
1272 <https://doi.org/10.3389/frsen.2021.748362>, 2021.

1273 Lyapustin, A., Wang, Y., Korkin, S., and Huang, D.: MODIS Collection 6 MAIAC algorithm, *Atmos. Meas. Tech.*, 11, 5741–  
1274 5765, <https://doi.org/10.5194/amt-11-5741-2018>, 2018.

1275 Nanda, S., de Graaf, M., Veefkind, J. P., Sneep, M., ter Linden, M., Sun, J., and Levelt, P. F.: A first comparison of TROPOMI  
1276 aerosol layer height (ALH) to CALIOP data, *Atmos. Meas. Tech.*, 13, 3043–3059, <https://doi.org/10.5194/amt-13-3043-2020>,  
1277 2020.

1278 Park, S. S., Kim, J., Cho, Y., Lee, H., Park, J., Lee, D.-W., Lee, W.-J., and Kim, D.-R.: Retrieval Algorithm for Aerosol Effective  
1279 Height from the Geostationary Environment Monitoring Spectrometer (GEMS), *Atmos. Meas. Tech. Discuss.*, <https://doi.org/10.5194/amt-223-136>.  
1280

1281 Powell, K. A., Hu, Y., Omar, A., Vaughan, M. A., Winker, D. M., Liu, Z., Hunt, W. H., and Young, S. A.: Overview of the  
1282 CALIPSO Mission and CALIOP Data Processing Algorithms, *J. Atmos. Ocean. Tech.*, 26, 2310–2323,  
1283 <https://doi.org/10.1175/2009jtecha1281.1>, 2009.

1284 Ram, K., Sarin, M.M., Sudheer, A.K., and Rengarajan, R.: Carbonaceous and Secondary Inorganic Aerosols during Wintertime  
1285 Fog and Haze over Urban Sites in the Indo-Gangetic Plain, *Aerosol Air Qual. Res.*, 41, 359–370,  
1286 <https://doi.org/10.4209/aaqr.2011.07.0105>, 2012.

1287 [Rodgers, C. D.: Inverse method for atmospheric sounding: theory and practice. World Scientific Publishing Co. Pte. Ltd.,](#)  
1288 [Singapore, 2000.](#)

1289 Sayer, A. M., Hsu, N. C., Lee, J., Carletta, N., Chen, S. H., and Smirnov, A.: Evaluation of NASA Deep Blue/SOAR aerosol  
1290 retrieval algorithms applied to AVHRR measurements, *J. Geophys. Res. Atmos.*, 122, 9945–9967,  
1291 <https://doi.org/10.1002/2017JD026934>, 2017.

1292 Singh, G. K., Choudhary, V., Rajeev, P., Paul, D., and Gupta, T.: Understanding the origin of carbonaceous aerosols during  
1293 periods of extensive biomass burning in northern India. *Environ. Pollut.*, 270, 116082,  
1294 <https://doi.org/10.1016/j.envpol.2020.116082>, 2021.

1295 Sinyuk, A., Holben, B. N., Eck, T. F., Giles, D. M., Slutsker, I., Korkin, S., Schafer, J. S., Smirnov, A., Sorokin, M., and  
1296 Lyapustin, A.: The AERONET Version 3 aerosol retrieval algorithm, associated uncertainties and comparisons to Version 2,  
1297 *Atmos. Meas. Tech.*, 13, 3375–3411, <https://doi.org/10.5194/amt-13-3375-2020>, 2020.

1298 Spurr, R. J. D.: VLIDORT: A linearized pseudo-spherical vector discrete ordinate radiative transfer code for forward model

- 1336 and retrieval studies in multilayer multiple scattering media, *J. Quant. Spectrosc. Radiat. Transf.*, 102, 316–342,  
 1337 <https://doi.org/10.1016/j.jqsrt.2006.05.005>, 2006.
- 1338 Taskinen, H., Väisänen, A., Hatakka, L., Virtanen, T. H., Lähivaara, T., Arola, A., Kolehmainen, V., and Lipponen, A.: High-  
 1339 Resolution Post-Process Corrected Satellite AOD, *Geophys. Res. Lett.*, 49, <https://doi.org/10.1029/2022gl099733>, 2022.
- 1340 Torres, O., Bhartia, P. K., Herman, J. R., Syniuk, A., Ginoux, P., and Holben, B.: A long term record of aerosol optical depth  
 1341 from TOMS observations D and comparison to AERONET measurements, *J. Atm. Sci.*, 59, 398–413, 2002.
- 1342 Torres, O., Ahn, C., and Chen, Z.: Improvements to the OMI near-UV aerosol algorithm using A-train CALIOP and AIRS  
 1343 observations, *Atmos. Meas. Tech.*, 6, 3257–3270, <https://doi.org/10.5194/amt-6-3257-2013>, 2013.
- 1344 Torres, O., Bhartia, P. K., Sinyuk, A., Welton, E. J., and Holben, B.: Total Ozone Mapping Spectrometer measurements of  
 1345 aerosol absorption from space: Comparison to SAFARI 2000 ground-based observations, *J. Geophys. Res.*, 110, D10S18,  
 1346 <https://doi.org/10.1029/2004JD004611>, 2005.
- 1347 Torres, O., Tanskanen, A., Veihelmann, B., Ahn, C., Braak, R., Bhartia, P. K., Veeffkind, P., and Levelt, P.: Aerosols and surface  
 1348 UV products from Ozone Monitoring Instrument observations: An overview, *J. Geophys. Res.*, 112,  
 1349 <https://doi.org/10.1029/2007jd008809>, 2007.
- 1350 Torres, O., Jethva, H., Ahn, C., Jaross, G., and Loyola, D. G.: TROPOMI aerosol products: evaluation and observations of  
 1351 synoptic-scale carbonaceous aerosol plumes during 2018–2020, *Atmos. Meas. Tech.*, 13, 6789–6806,  
 1352 <https://doi.org/10.5194/amt-13-6789-2020>, 2020.
- 1353 Wei, J., Li, Z., Sun, L., Peng, Y., Zhang, Z., Li, Z., Su, T., Feng, L., Cai, Z., and Wu, H.: Evaluation and uncertainty estimate  
 1354 of next-generation geostationary meteorological Himawari-8/AHI aerosol products, *Sci. Total Environ.*, 692, 879–891,  
 1355 <https://doi.org/10.1016/j.scitotenv.2019.07.326>, 2019.
- 1356 Xu, X., Wang, J., Wang, Y., Zeng, J., Torres, O., Reid, J. S., Miller, S. D., Martins, J. V., and Remer, L. A.: Detecting layer  
 1357 height of smoke aerosols over vegetated land and water surfaces via oxygen absorption bands: hourly results from  
 1358 EPIC/DSCOVR in deep space, *Atmos. Meas. Tech.*, 12, 3269–3288, <https://doi.org/10.5194/amt-12-3269-2019>, 2019.
- 1359 Xu, X., Wang, J., Wang, Y., Zeng, J., Torres, O., Yang, Y., Marshak, A., Reid, J., and Miller, S.: Passive remote sensing of  
 1360 altitude and optical depth of dust plumes using the oxygen A and B bands: first results from EPIC/DSCOVR at Lagrange-1  
 1361 point, *Geophys. Res. Lett.*, 44, 7544–7554, <https://doi.org/10.1002/2017gl073939>, 2017.
- 1362 Yin, S., Wang, X., Zhang, X., Guo, M., Miura, M., and Xiao, Y.: Influence of biomass burning on local air pollution in mainland  
 1363 Southeast Asia from 2001 to 2016, *Environ. Pollut.*, 254, 112949, <https://doi.org/10.1016/j.envpol.2019.07.117>, 2019.
- 1364 Yoshida, M., Kikuchi, M., Nagao, T. M., Murakami, H., Nomaki, T., and Higurashi, A.: Common Retrieval of Aerosol  
 1365 Properties for Imaging Satellite Sensors, *J. Meteorol. Soc. Jpn. Ser. II*, 96B, 193–209, <https://doi.org/10.2151/jmsj.2018-039>,  
 1366 2018.
- 1367 Zhang, H., Kondragunta, S., Laszlo, I., and Zhou, M.: Improving GOES Advanced Baseline Imager (ABI) aerosol optical  
 1368 depth (AOD) retrievals using an empirical bias correction algorithm, *Atmos. Meas. Tech.*, 13, 5955–5975,  
 1369 <https://doi.org/10.5194/amt-13-5955-2020>, 2020.
- 1370 Zhang, H., Kondragunta, S., Laszlo, I., Liu, H., Remer, L. A., Huang, J., Superczynski, S., and Ciren, P.: An enhanced VIIRS  
 1371 aerosol optical thickness (AOT) retrieval algorithm over land using a global surface reflectance ratio database, *J. Geophys.*  
 1372 *Res. Atmos.*, 121, <https://doi.org/10.1002/2016jd024859>, 2016.

1373 Zhang, W., Gu, X., Xu, H., Yu, T., and Zheng, F.: Assessment of OMI near-UV aerosol optical depth over Central and East  
1374 Asia, *J. Geophys. Res. Atmos.*, 121, 382–398, <https://doi.org/10.1002/2015jd024103>, 2016.

1375 Zhang, Z., Wu, W., Fan, M., Tao, M., Wei, J., Jin J., Tan, Y. and Wang, Q.: Validation of Himawari-8 aerosol optical depth  
1376 retrievals over China, *Atmos. Environ.*, 199, <https://doi.org/10.1016/j.atmosenv.2018.11.024>, 2019.

1377  
|



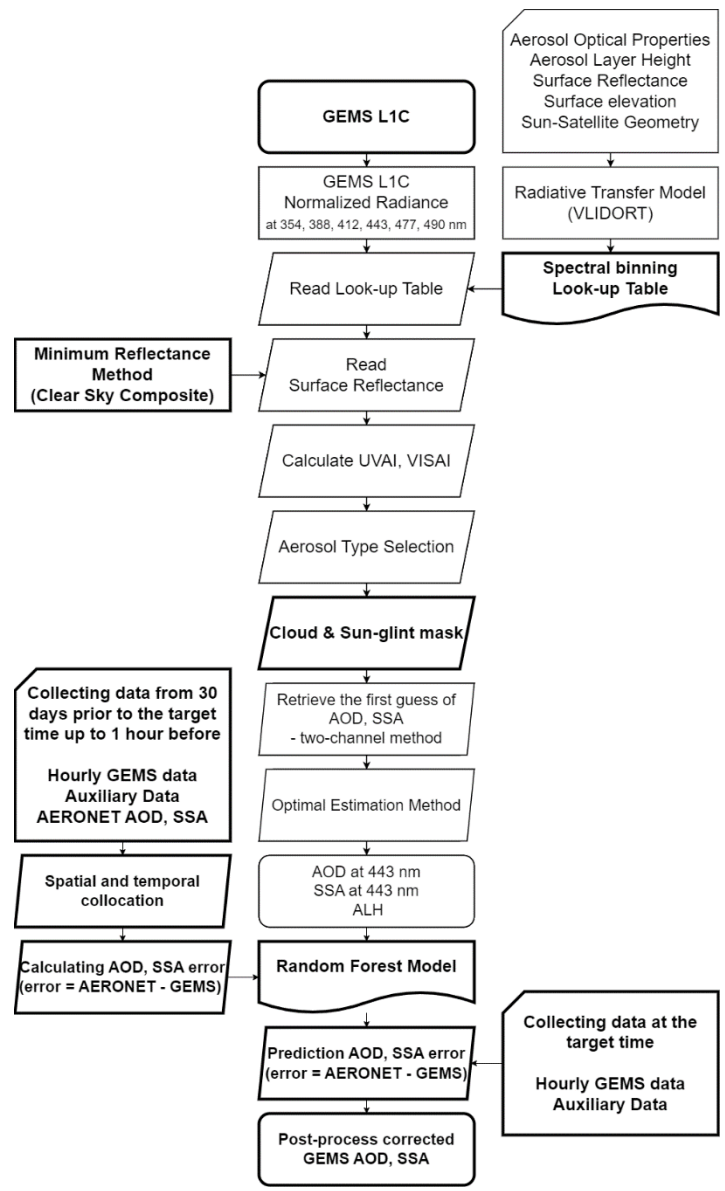
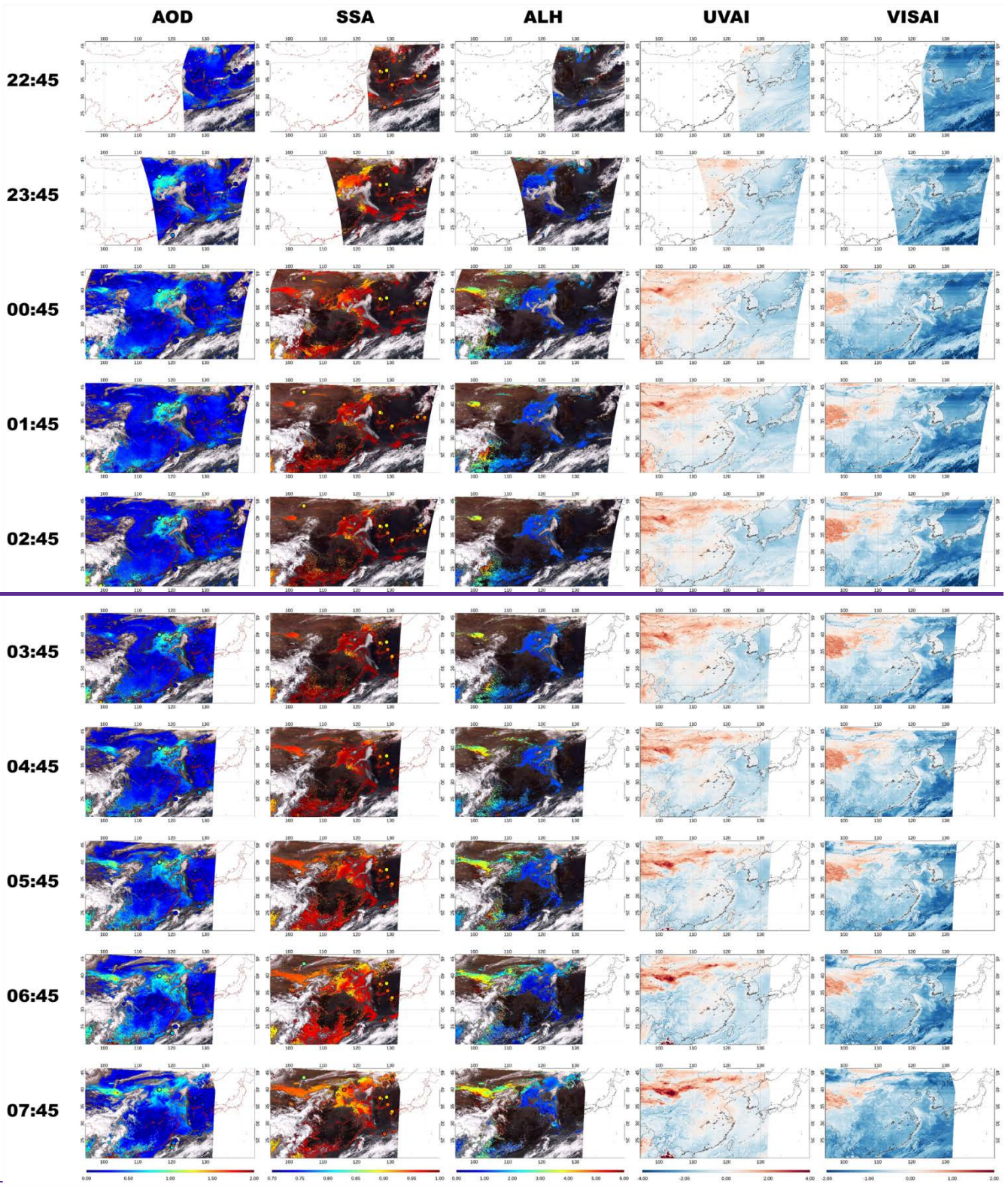
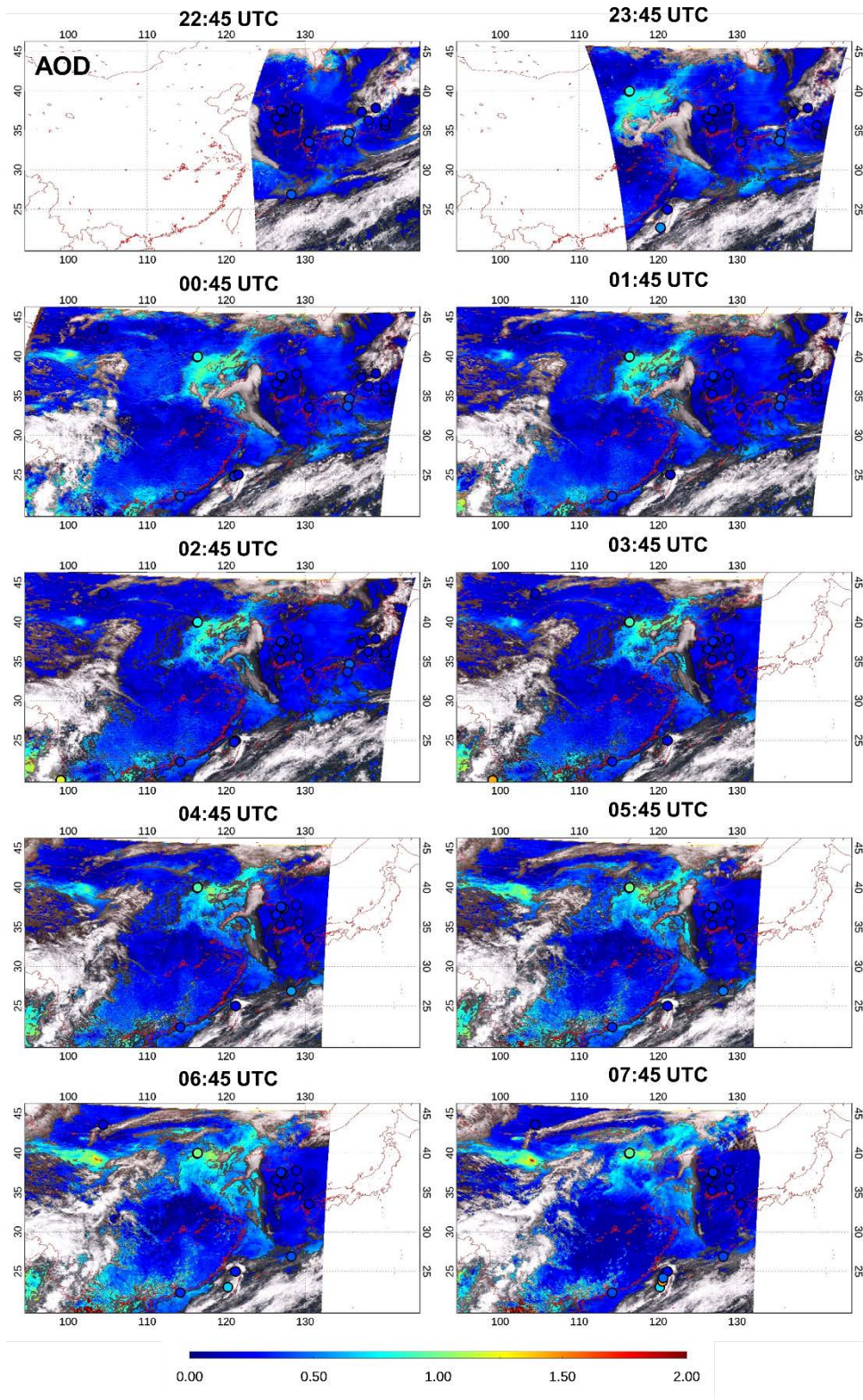


Figure 1: The flowchart of the GEMS AERAOD retrieval algorithm and the modifications in the study (in bold boxes)



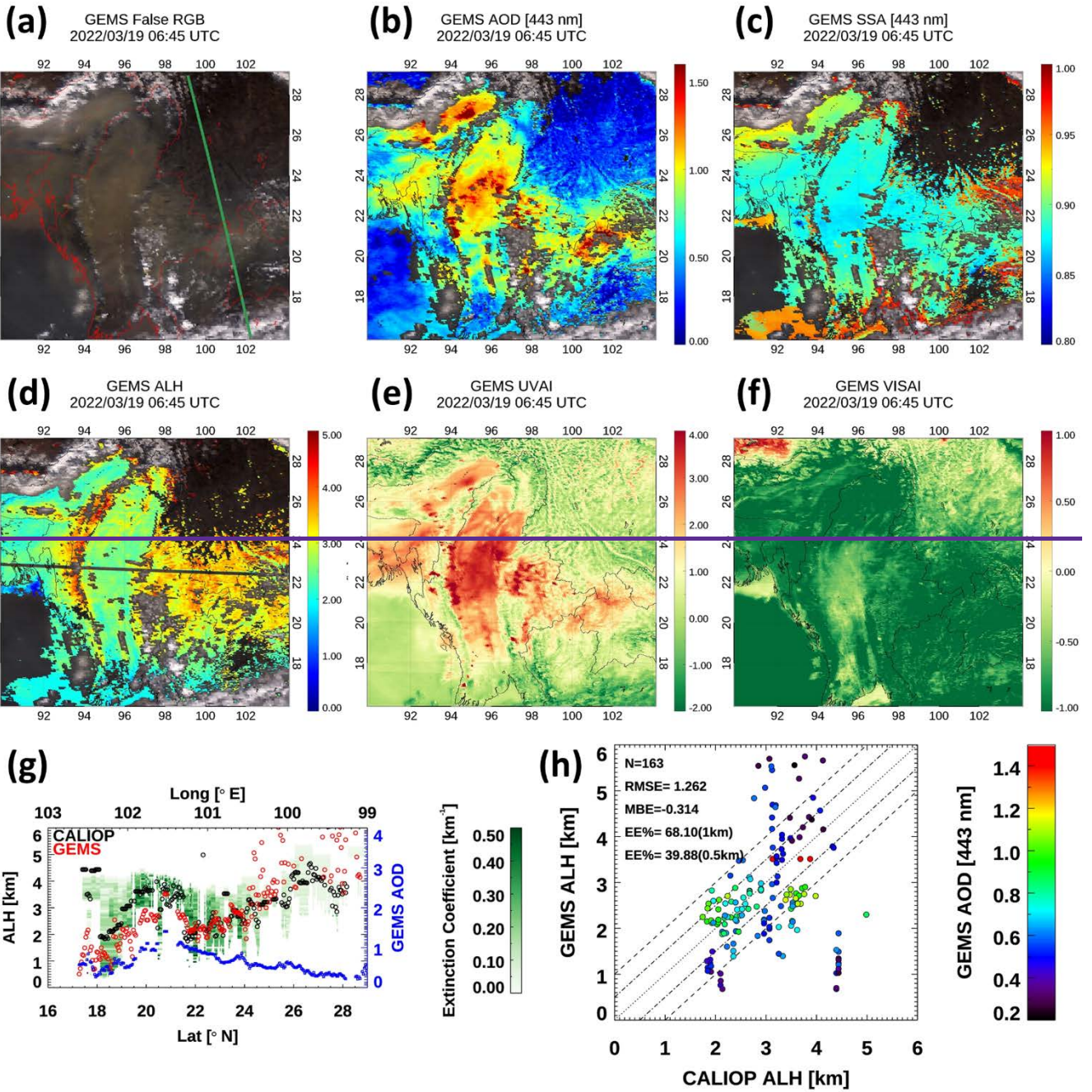
1388





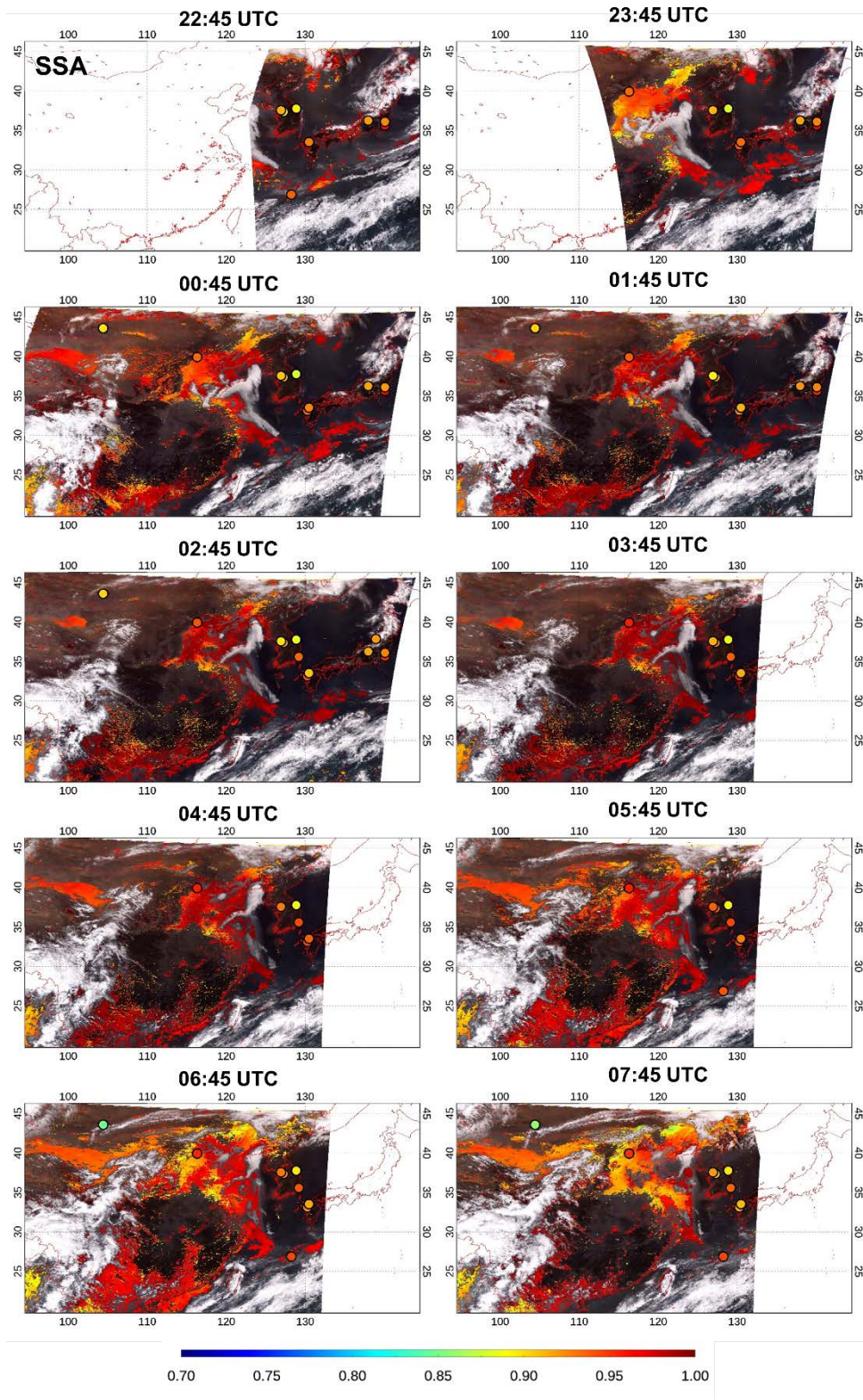
1389  
 1390 **Figure 2: Hourly GEMS aerosol products for the dust case on April 8, 2022 over northwestern China. Time-series maps of AOD at**  
 1391 **443 nm, SSA, ALH, UVAI at 443 nm, and VISALH (km) from 22:45 UTC to 07:45 UTC. The circle denotes an AERONET**  
 1392 **station, and the filled color indicates the AERONET AOD and SSA at 443 nm in the AOD and SSA columns. GEMS SSA, and ALH**  
 1393 **are displayed only when GEMS AOD > 0.2.**





1395  
1396



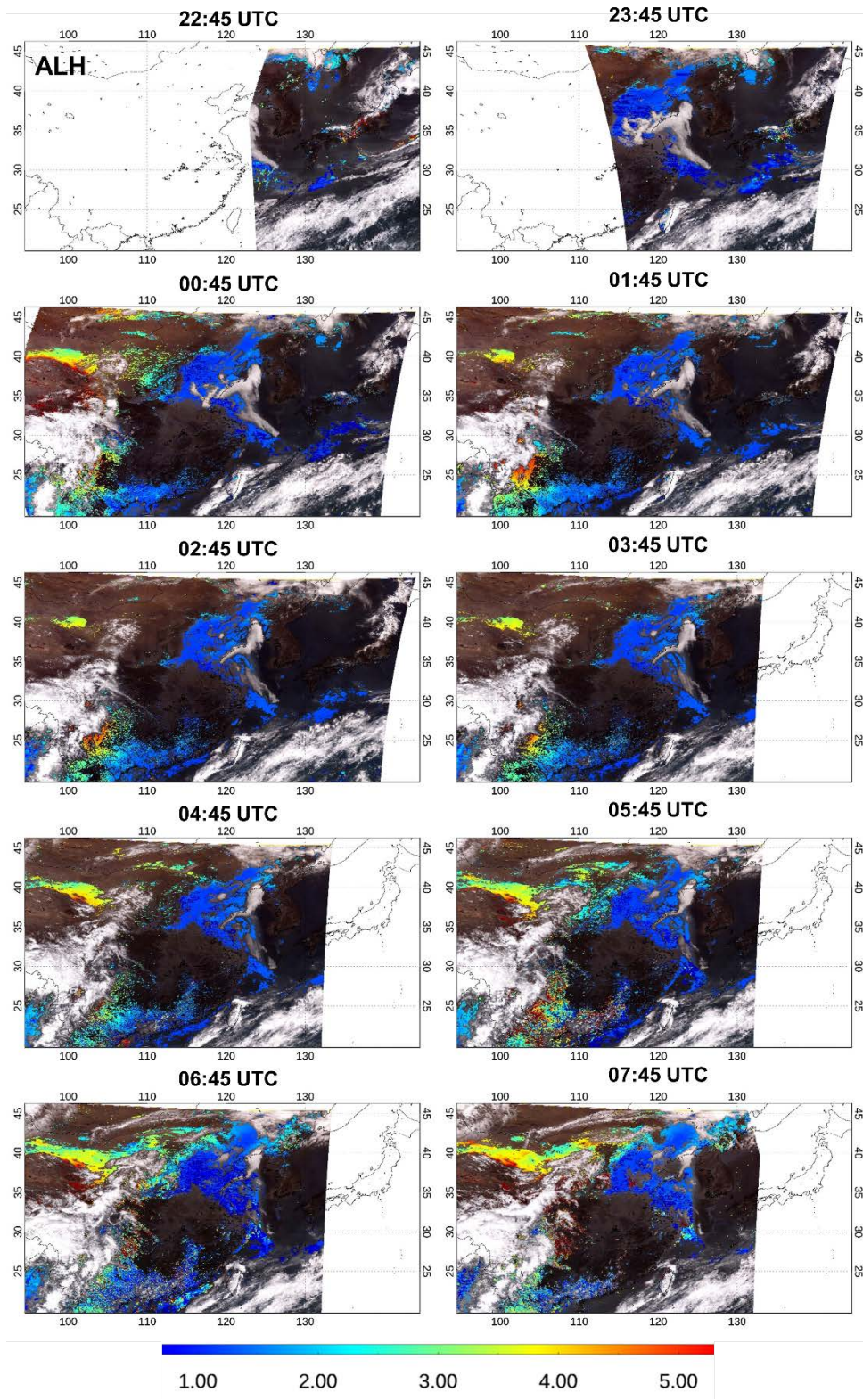


1397

1398

Figure 2: Continue





1399

1400

1401

Figure 2: Continue



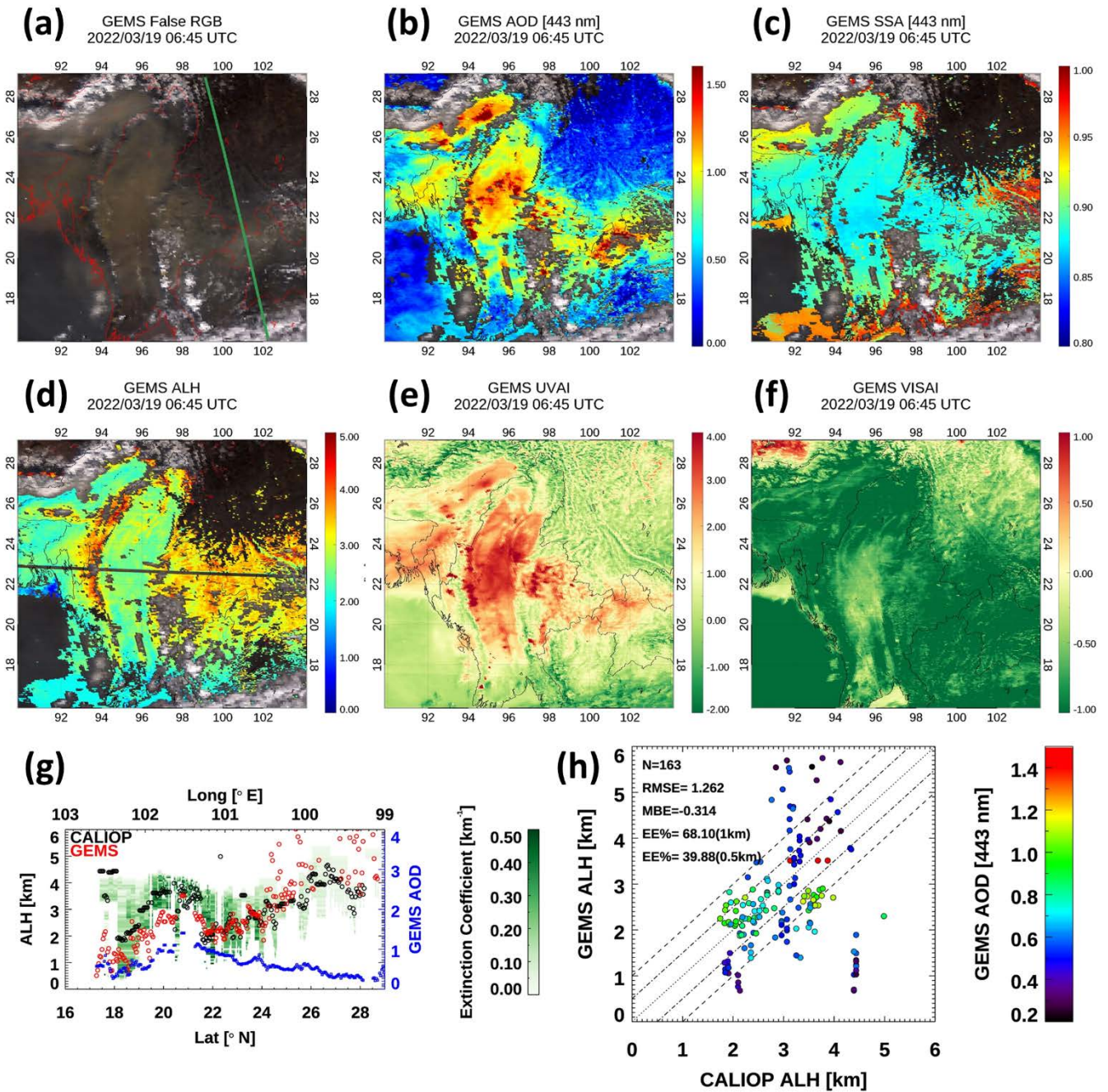
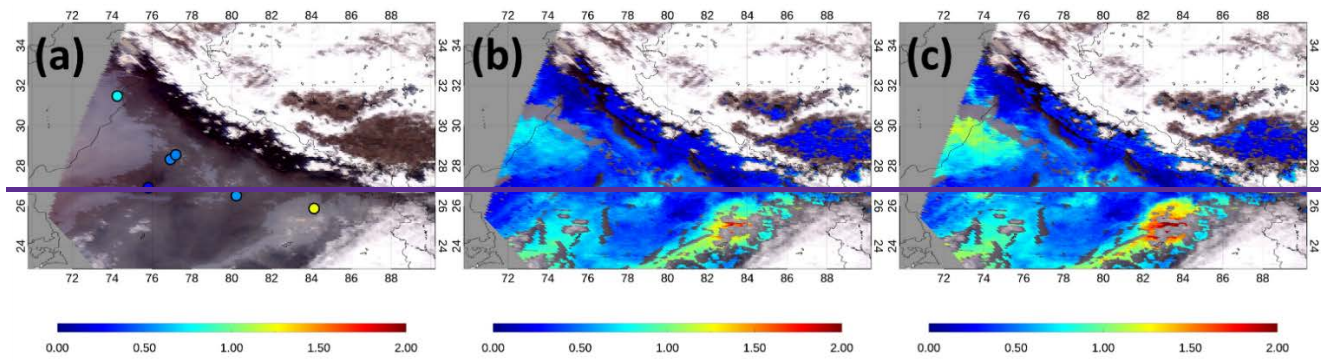
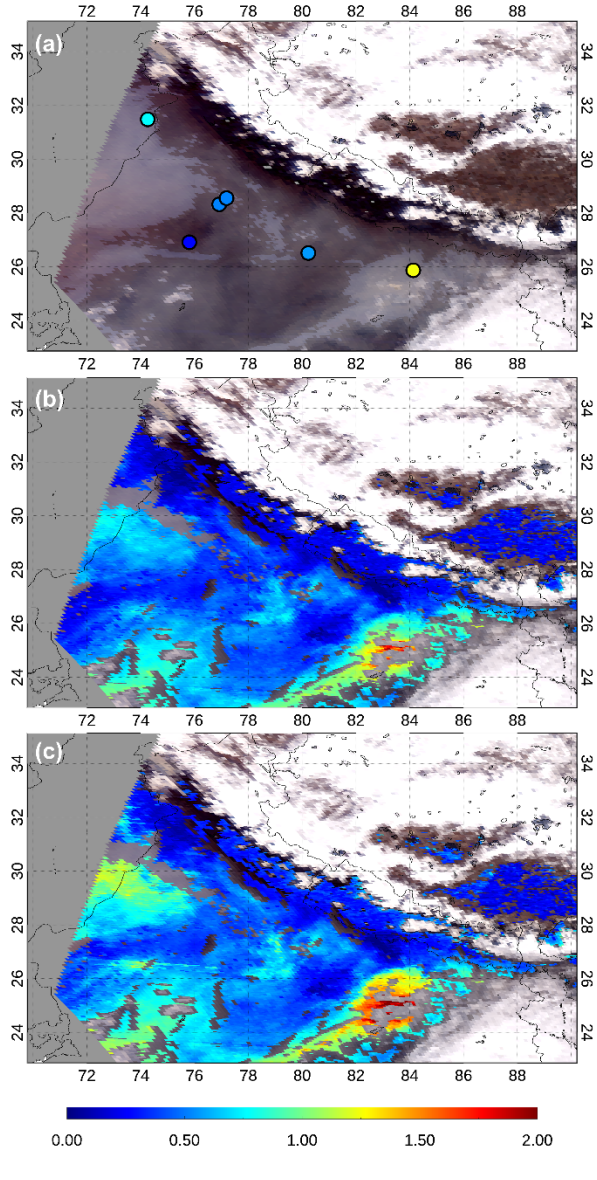


Figure 3: The example of GEMS aerosol products for biomass burning over mainland Southeast Asia. The maps of- (a) GEMS False RGB, (b) AOD, (c) SSA, (d) ALH, (e) UVAI, and (f) VisAI. The green line in GEMS False RGB indicates the overpass path of CALIOP. The GEMS SSA and ALH are displayed only when the GEMS AOD is over 0.2. (g) GEMS ALH compared with CALIOP extinction coefficient in the domain. The background color represents the CALIOP extinction coefficient. The black open circles denote the CALIOP ALH, whereas the red open circles represent the GEMS ALH. The blue squares represent the GEMS AOD. (h) Comparison of GEMS and CALIOP ALH when GEMS AOD > 0.2. The dashed and dash-dotted lines indicate an uncertainty envelope of  $\pm 1$  km and  $\pm 0.5$  km in ALH, respectively. The dotted lines represent the 1:1 line. The color in the circles represents the GEMS AOD.



1434



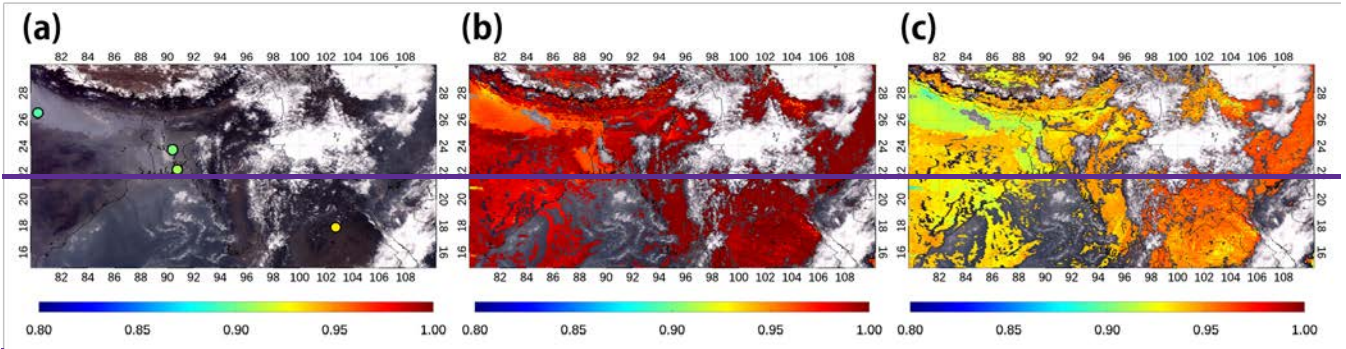
1435

1436 **Figure 4: The example of the GEMS AOD before and after post-processing for an absorbing aerosol case over Indo-Gangatic Plane**  
 1437 **at 04:45 UTC on December 4, 2021. (a) GEMS false RGB. The circle denotes an AERONET station, and the filled color indicates**  
 1438 **the AERONET AOD at 443 nm, (b) GEMS AOD<sub>2</sub> and (c) GEMS AOD after post-process correction.**

1439



1447



1448

1449

1450

1451

1452

1453

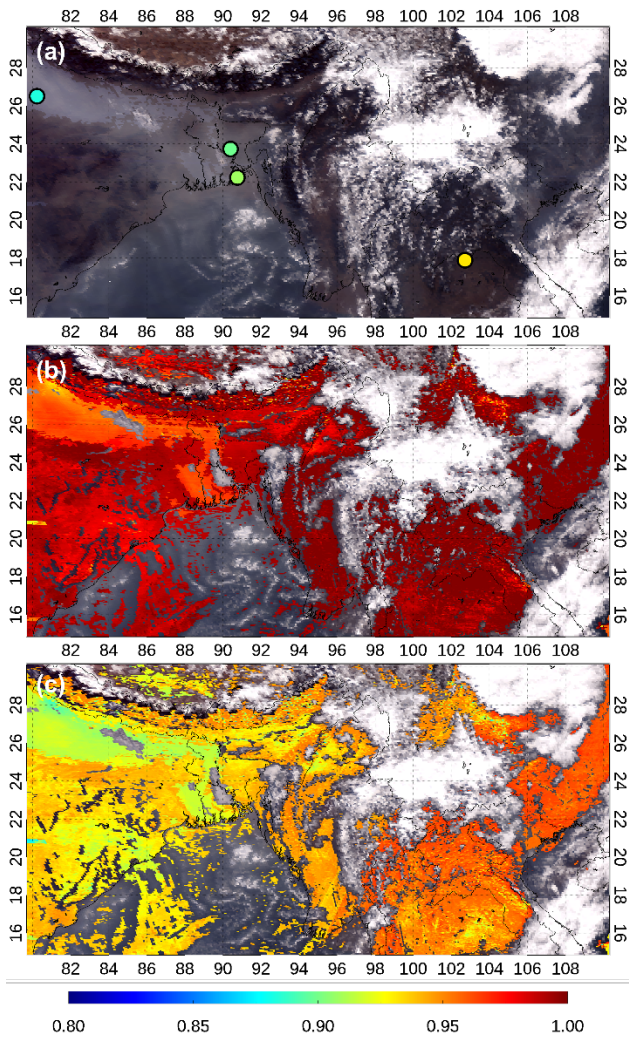


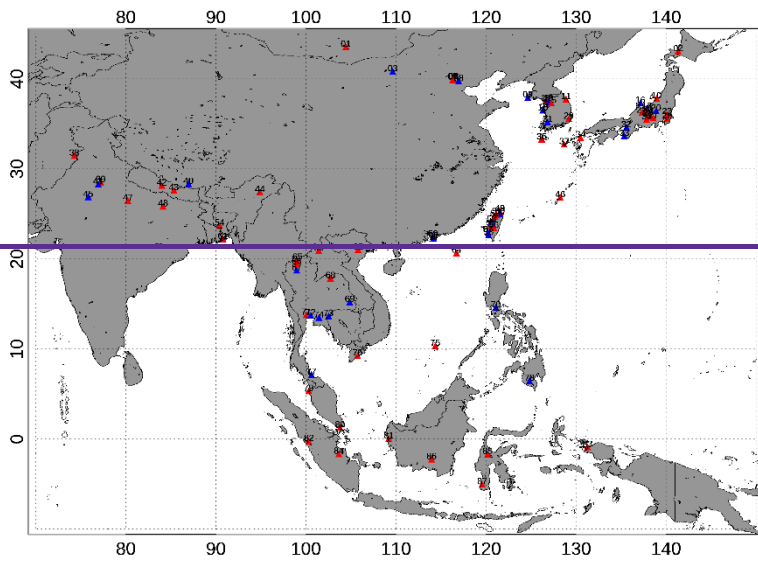
Figure 5: The example of GEMS SSA and the GEMS SSA after post-processing for an absorbing aerosol case over India,

Bangladesh, and mainland Southeast Asia at 03:45 UTC on December 23, 2021. (a) GEMS false RGB. The circle denotes an

AERONET station, and the filled color indicates the AERONET SSA at 440 nm, (b) GEMS SSA, and (c) GEMS SSA after post-

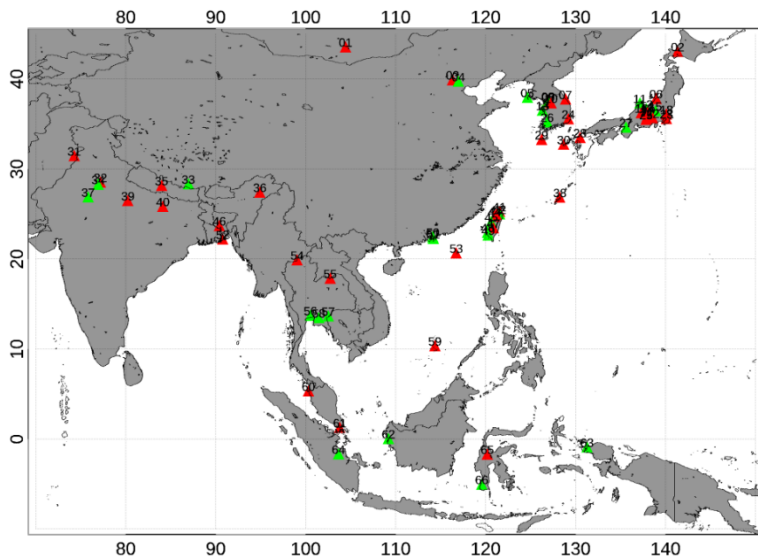
process correction.

AERONET sites used for the GEMS AOD and SSA validation



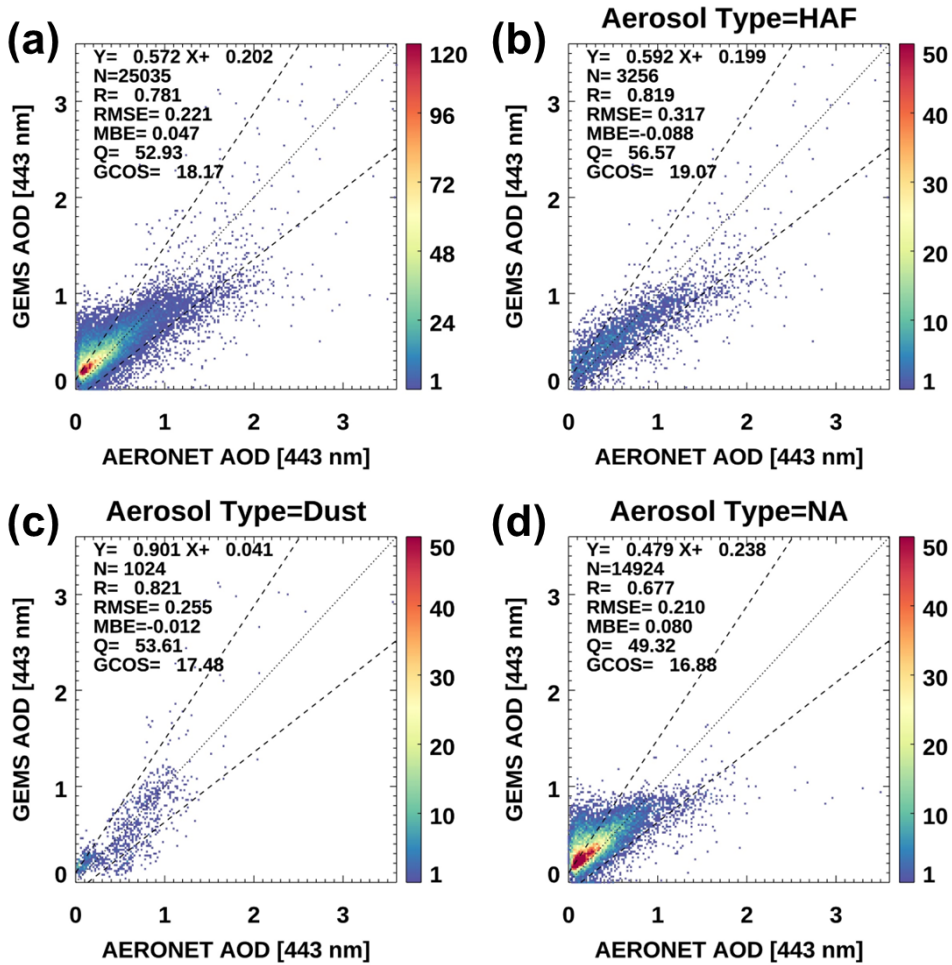
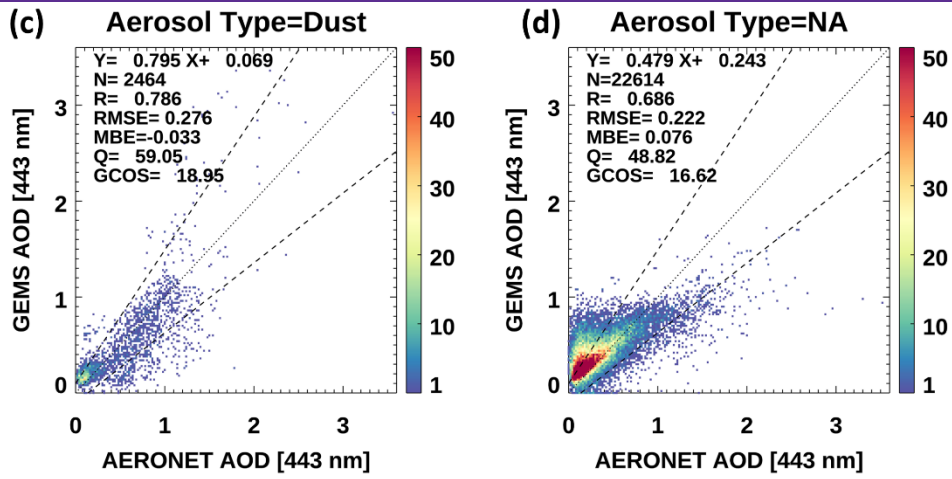
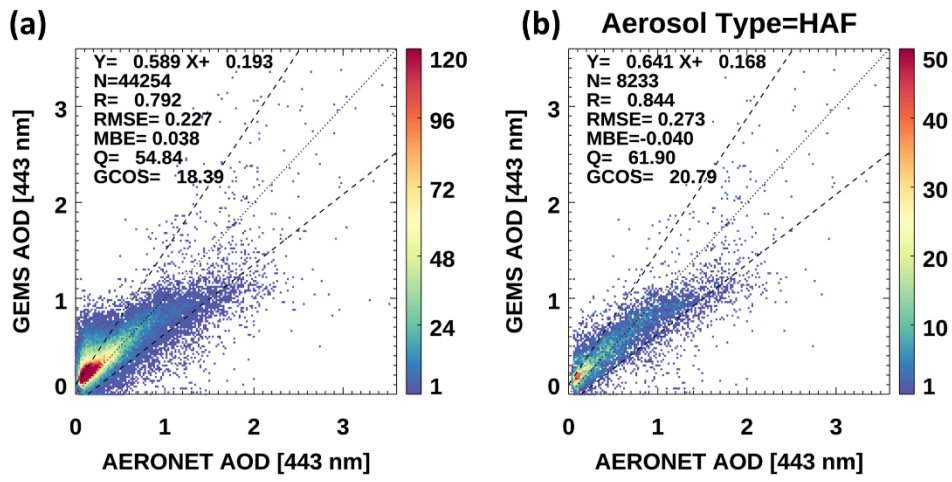
- 01:Dalanzadgad( 915, 686)
- 02:Hokkaido\_University(345, 188)
- 03:AOE\_Baotou( 828, 0)
- 04:Beijing\_RAD1(1229, 0)
- 05:Beijing\_PKU( 464, 222)
- 06:Beijing(1099, 0)
- 07:Beijing-CAMS(1469,1154)
- 08:XiangHe( 719, 0)
- 09:Baengnyeong( 427, 0)
- 10:Niigata( 342, 197)
- 11:Gangneung\_WNU(1260, 759)
- 12:Incheon( 422, 303)
- 13:Yonsei\_University(1053, 781)
- 14:Seoul\_SNU(1046, 0)
- 15:Hankuk\_UFS( 997, 501)
- 16:Noto( 299, 0)
- 17:DRAGON\_Hakuba( 5, 0)
- 18:Anmyon( 958, 0)
- 19:DRAGON\_Omachi( 7, 2)
- 20:DRAGON\_Mt\_Haruna( 2, 0)
- 21:DRAGON\_Takayama( 31, 12)
- 22:DRAGON\_Matsumoto( 377, 201)
- 23:TGF\_Tsukuba( 215, 174)
- 24:DRAGON\_Suwa( 10, 6)
- 25:DRAGON\_Minowa( 74, 49)
- 26:DRAGON\_Ina( 71, 51)
- 27:DRAGON\_Kofu( 301, 223)
- 28:Chiba\_University( 471, 336)
- 29:KORUS\_UNIST\_Ulsan(1245, 861)
- 30:DRAGON\_Iida( 72, 35)
- 31:Gwangju\_GIST(603, 0)
- 32:Osaka( 383, 0)
- 33:Shirahama( 574, 0)
- 34:Fukuoka(1002, 515)
- 35:Gosan\_NIMS\_SNU( 148, 94)
- 36:Gosan\_SNU( 293, 101)
- 37:Fukue( 241, 129)
- 38:Lahore( 842, 629)
- 39:IIT\_Delhi( 579, 456)
- 40:QOMS\_CAS( 326, 0)
- 41:Amity\_Univ\_Gurgaon( 586, 0)
- 42:Pokhara( 399, 249)
- 43:ICIMOD( 107, 77)
- 44:Dibrugarh\_Univ(473, 301)
- 45:Jaipur( 54, 0)
- 46:Okinawa\_Hedof( 802, 285)
- 47:Kanpur( 610, 447)
- 48:Gandhi\_College( 411, 275)
- 49:Cape\_Fuguei\_Station(208, 87)
- 50:Taipei\_CWB( 433, 0)
- 51:EPA-NCU( 757, 296)
- 52:TASA\_Taiwan( 771, 325)
- 53:Xitun( 563, 0)
- 54:Dhaka\_University( 636, 370)
- 55:Douliu(1033, 403)
- 56:Lulin( 576, 159)
- 57:Chen-Kung\_Univ( 807, 0)
- 58:Kaohsiung( 818, 0)
- 59:Hong\_Kong\_Sheung( 30, 0)
- 60:Hong\_Kong\_PolyU( 597, 0)
- 61:Bhola( 488, 304)
- 62:NGHIA\_DO( 182, 66)
- 63:Luang\_Namtha( 282, 60)
- 64:Dongsha\_Island( 219, 85)
- 65:Doi\_Ang\_Khang( 436, 210)
- 66:Chiang\_Dao( 576, 145)
- 67:Chiang\_Mai\_Met\_Sta( 806, 0)
- 68:Nong\_Khai( 604, 256)
- 69:Ubon\_Ratchathani( 1, 0)
- 70:Manila\_Observatory( 28, 0)
- 71:Silpakorn\_Univ( 530, 180)
- 72:Bangkok( 256, 0)
- 73:Sra\_Kaeo( 397, 0)
- 74:Chachoengsao( 321, 0)
- 75:Tai\_Ping( 50, 9)
- 76:Bac\_Lieu( 236, 24)
- 77:Songkha\_Met\_Sta( 110, 0)
- 78:ND\_Marbel\_Univ( 281, 0)
- 79:USM\_Penang( 350, 88)
- 80:Singapore( 413, 64)
- 81:Pontianak( 780, 133)
- 82:Bukit\_Kotabang( 283, 59)
- 83:Surong( 166, 20)
- 84:Jambi( 222, 3)
- 85:BMKG\_GAW\_PALU( 130, 10)
- 86:Palangkaraya( 400, 33)
- 87:Makassar( 130, 8)

AERONET sites used for the GEMS AOD and SSA validation



- 01:Dalanzadgad( 502, 227)
- 02:Hokkaido\_University( 345, 128)
- 03:Beijing-CAMS( 291, 137)
- 04:XiangHe( 334, 0)
- 05:Baengnyeong( 427, 0)
- 06:Niigata( 342, 116)
- 07:Gangneung\_WNU(1181, 353)
- 08:Yonsei\_University(1053, 399)
- 09:Seoul\_SNU(1035, 0)
- 10:Hankuk\_UFS( 997, 214)
- 11:Noto( 299, 0)
- 12:DRAGON\_Hakuba( 5, 0)
- 13:Anmyon( 763, 0)
- 14:DRAGON\_Omachi( 7, 0)
- 15:DRAGON\_Mt\_Haruna( 2, 0)
- 16:DRAGON\_Takayama( 31, 2)
- 17:DRAGON\_Matsumoto( 440, 203)
- 18:TGF\_Tsukuba( 270, 142)
- 19:DRAGON\_Suwa( 10, 4)
- 20:DRAGON\_Minowa( 74, 32)
- 21:DRAGON\_Ina( 71, 42)
- 22:DRAGON\_Kofu( 312, 78)
- 23:Chiba\_University( 470, 152)
- 24:KORUS\_UNIST\_Ulsan(1125, 612)
- 25:DRAGON\_Iida( 72, 29)
- 26:Gwangju\_GIST( 428, 0)
- 27:Osaka( 383, 0)
- 28:Fukuoka( 998, 375)
- 29:Gosan\_NIMS\_SNU( 148, 69)
- 30:Fukue( 240, 38)
- 31:Lahore( 842, 409)
- 32:IIT\_Delhi( 101, 90)
- 33:QOMS\_CAS( 327, 0)
- 34:Amity\_Univ\_Gurgaon( 607, 0)
- 35:Pokhara( 333, 119)
- 36:Dibrugarh\_Univ( 472, 214)
- 37:Jaipur( 54, 0)
- 38:Okinawa\_Hedof( 874, 133)
- 39:Kanpur( 114, 86)
- 40:Gandhi\_College( 96, 78)
- 41:Cape\_Fuguei\_Station( 53, 33)
- 42:Taipei\_CWB( 433, 0)
- 43:EPA-NCU( 267, 121)
- 44:TASA\_Taiwan( 680, 157)
- 45:Xitun( 579, 0)
- 46:Dhaka\_University( 651, 220)
- 47:Lulin( 575, 16)
- 48:Chen-Kung\_Univ( 792, 0)
- 49:Kaohsiung( 957, 0)
- 50:Hong\_Kong\_Sheung( 30, 0)
- 51:Hong\_Kong\_PolyU( 603, 0)
- 52:Bhola( 485, 256)
- 53:Dongsha\_Island( 219, 28)
- 54:Doi\_Ang\_Khang( 147, 40)
- 55:Nong\_Khai( 603, 104)
- 56:Bangkok( 256, 0)
- 57:Sra\_Kaeo( 394, 0)
- 58:Chachoengsao( 239, 0)
- 59:Tai\_Ping( 43, 1)
- 60:USM\_Penang( 347, 30)
- 61:Singapore( 413, 8)
- 62:Pontianak( 39, 0)
- 63:Surong( 163, 0)
- 64:Jambi( 222, 0)
- 65:BMKG\_GAW\_PALU( 134, 5)
- 66:Makassar( 19, 0)

Figure 6: AERONET sites used for the GEMS AOD and SSA validation. The red color indicates the site where validation points exist for both AOD and SSA. The blue/green color indicates the site where validation points exist only for AOD. The list of station names in conjunction with the number of AERONET AOD and SSA data points for validation at each station.



1466

1467



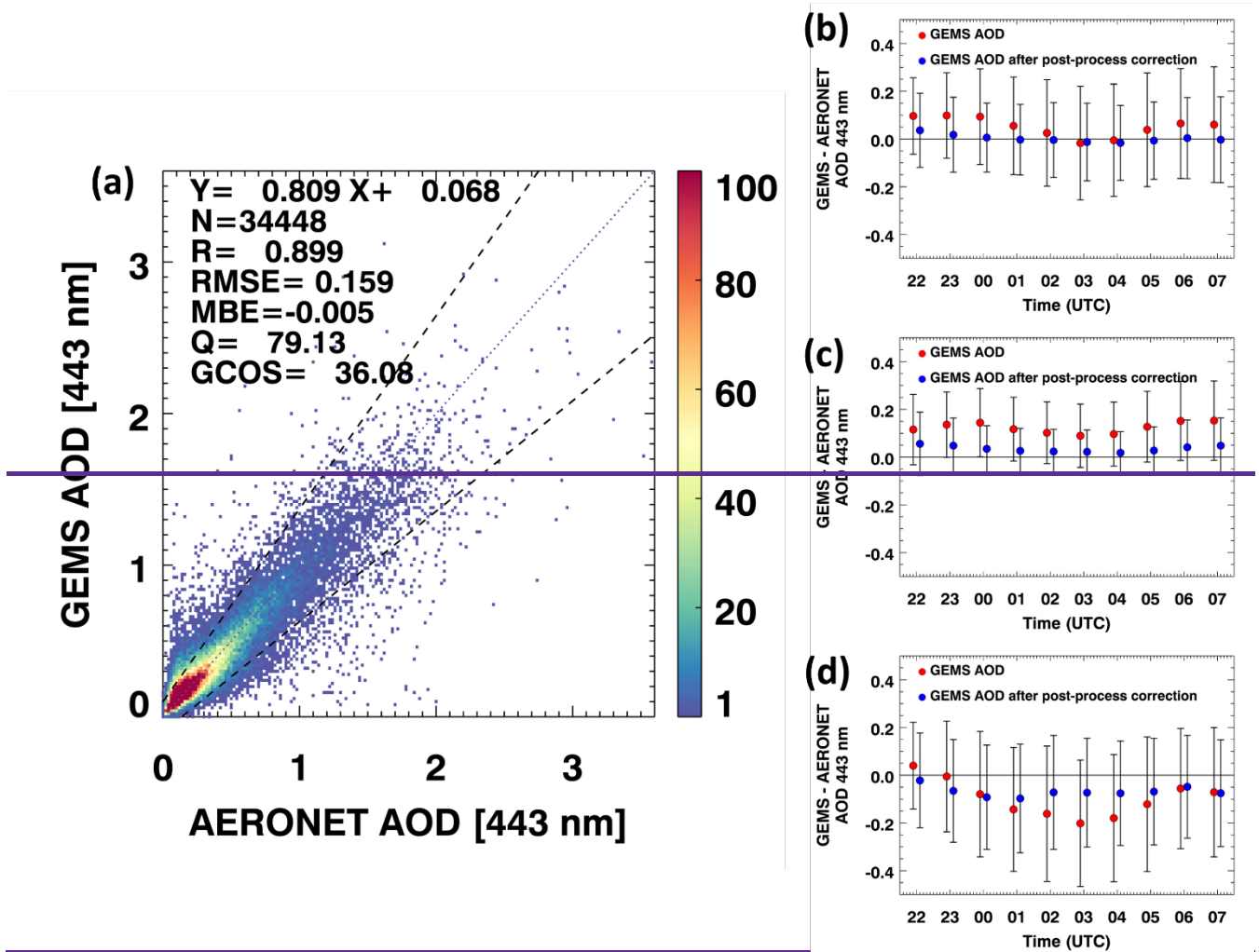
1472  
1473  
1474  
1475

**Figure 7: Comparison of GEMS and AERONET AOD for (a) total and individual aerosol types: (b) HAF, (c) dust, and (d) NA. The dashed lines indicate an uncertainty envelope of maximum (0.1 or 30%) in AOD. The dotted lines represent the 1:1 line. Data from November 1, 2021, to October 31, 2022, are used for comparison.**

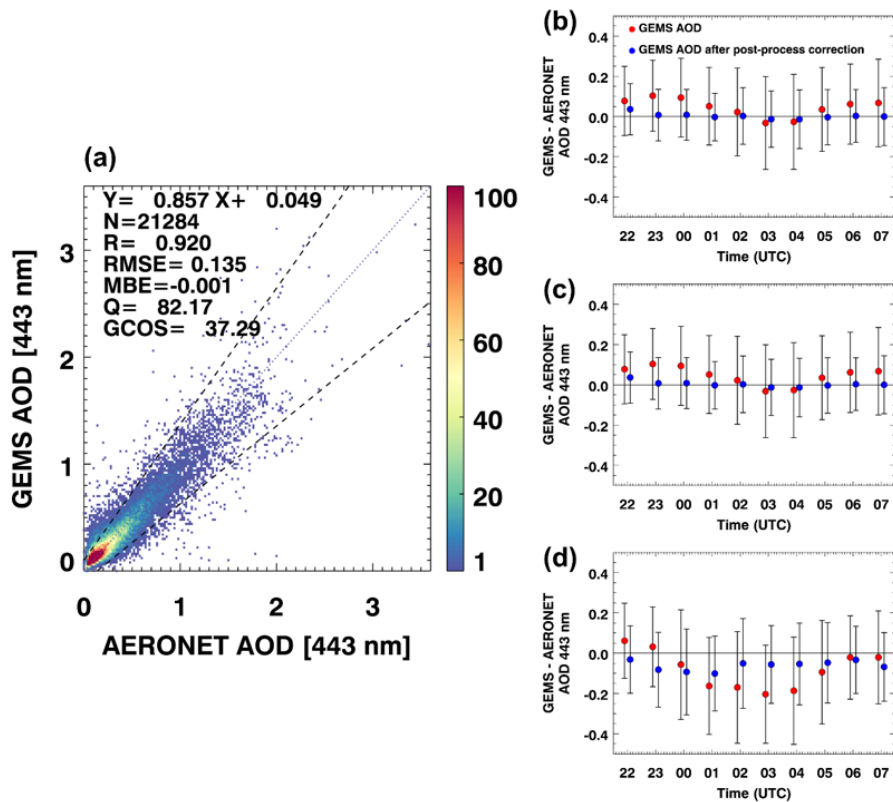


서

1476



1477



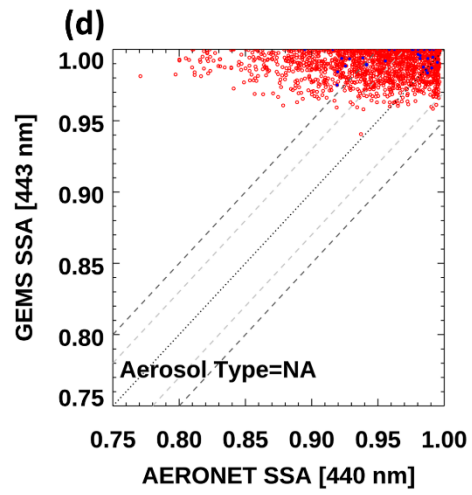
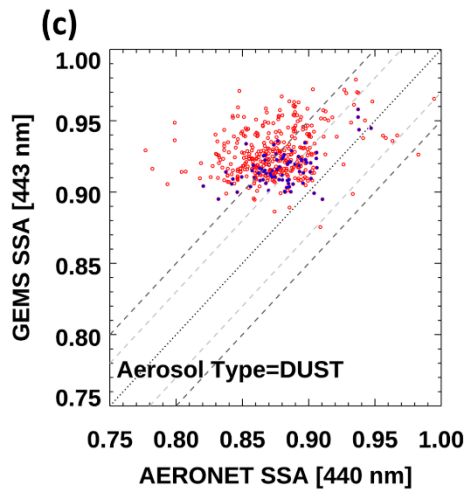
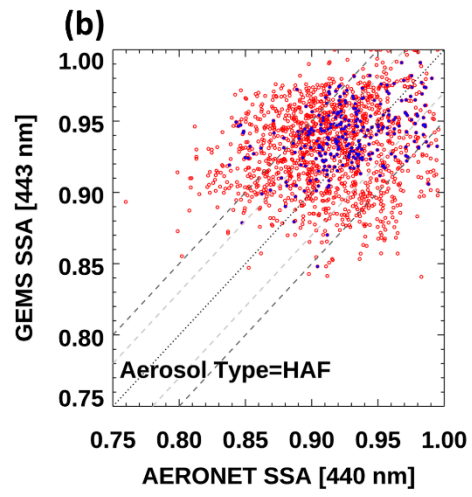
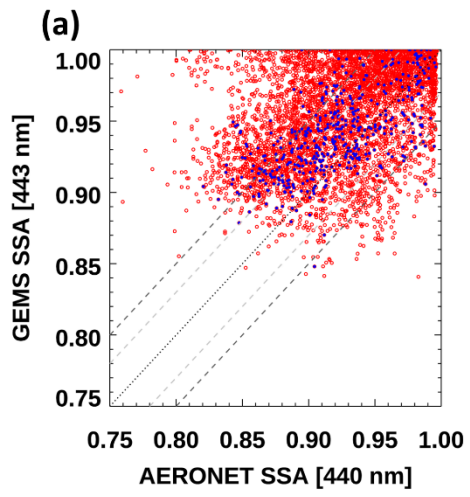
1478  
1479

Figure 8: (a) Comparison of GEMS AOD after post-process correction by machine learning and AERONET AOD. The dashed lines indicate an uncertainty envelope of a larger 0.1 or  $\pm 30\%$  in AOD. The dotted lines represent the 1:1 line. The difference

1485 between GEMS AOD and AERONET AOD in terms of time. (b) All pixels, (c) pixels when AERONET AOD < 0.4, and (d) pixels  
1486 when AERONET AOD > 0.4. The red circles represent the GEMS AOD, and the blue circles represent the GEMS AOD after post-  
1487 process correction. The error bars correspond to the standard deviation. Data from ~~December~~November 1, 2021, to October 31,  
1488 2022, are used for comparison.

1489

서식



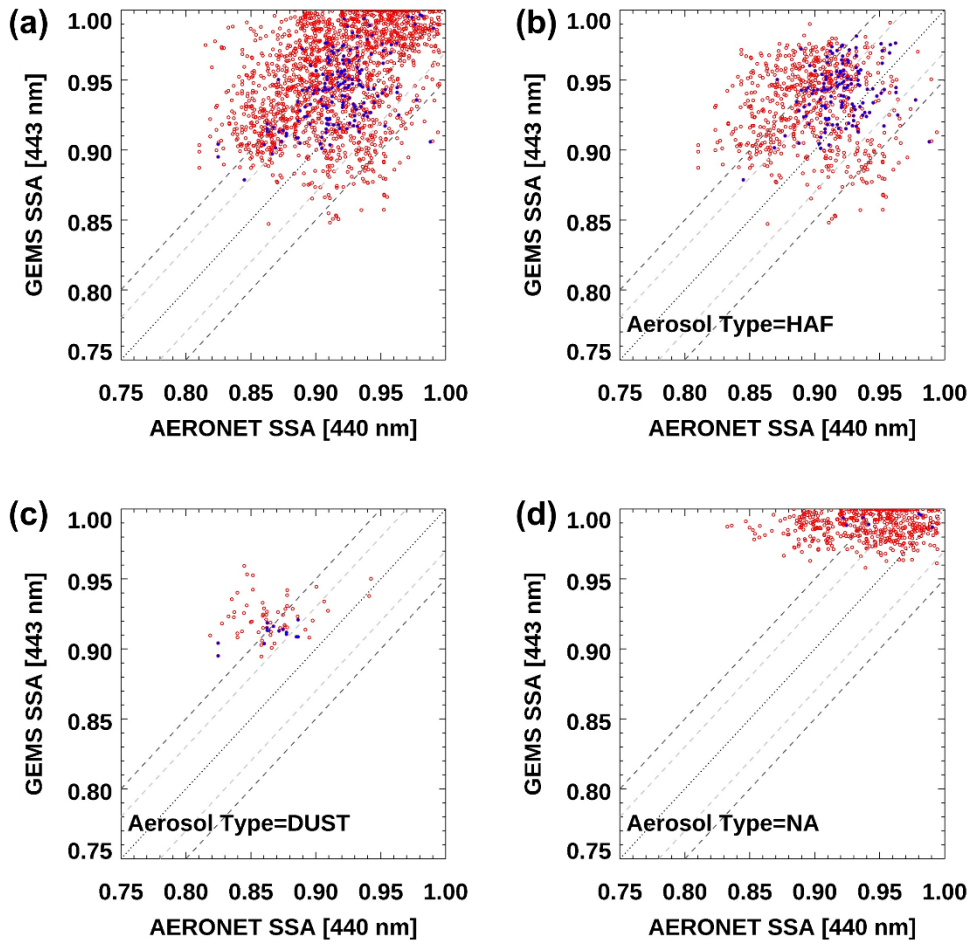


Figure 9: Comparison of GEMS and AERONET SSA for (a) total and individual aerosol types: (b) HAF, (c) dust, and (d) NA. The red circles represent the pixels when AOD > 0.4, and the blue circles represent the pixels when AOD > 1.0. The gray dashed lines indicate an uncertainty envelope of  $\pm 0.03$  in SSA, the black dashed lines indicate an uncertainty envelope of  $\pm 0.05$  in SSA, and the dotted lines represent the 1:1 line. Data from November 1, 2021, to October 31, 2022, are used for comparison.



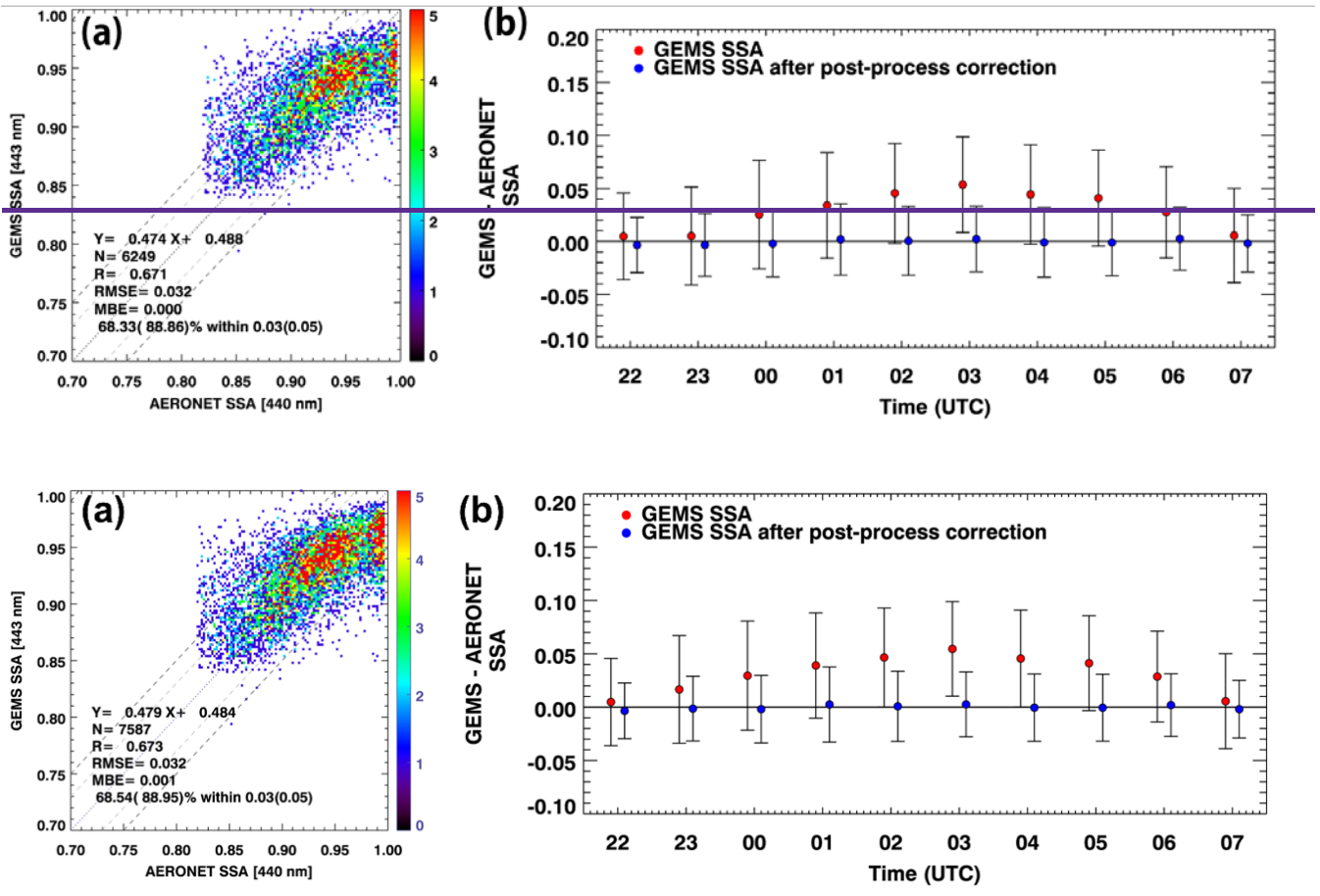


Figure 10: (a) Comparison of GEMS SSA after post-process correction and AERONET SSA. The gray dashed lines indicate an uncertainty envelope of  $\pm 0.03$  in SSA, the black dashed lines indicate an uncertainty envelope of  $\pm 0.05$  in SSA, and the dotted lines represent the 1:1 line. (b) The difference between GEMS and AERONET SSA in terms of time. Data from ~~December~~ November 1, 2021 to October 31, 2022 are used for comparison.

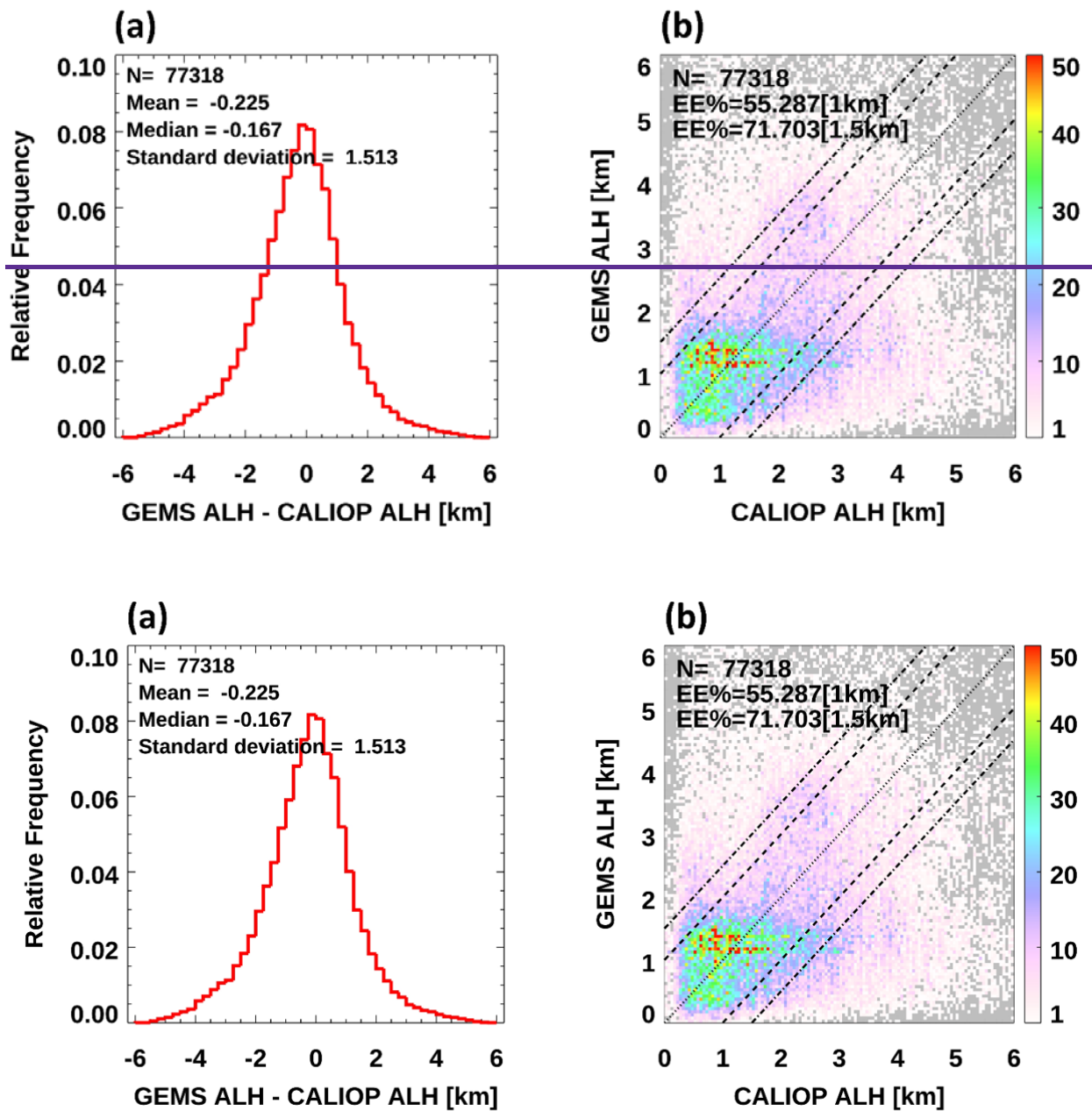


Figure 11: (a) Histogram of difference between GEMS and CALIOP ALH and (b) comparison of GEMS and CALIOP ALH. The dashed lines indicate an uncertainty envelope of  $\pm 1$  km in ALH. The dash-dotted lines indicate an uncertainty envelope of  $\pm 1.5$  km in ALH. The dotted lines represent the 1:1 line. Data from November 1, 2021, to October 31, 2022, are used for comparison.

Table 1: Dimension of LUT in GEMS Aerosol algorithm.

Variable Name [Unit]	Number of Entries	Entries
Wavelength [nm]	6	354, 388, 412, 443, 477, 490
SZA [°]	12	0.01, 5, 10, 15, 20, 27, 34, 41, 48, 55, 62, 69
VZA [°]	12	0.01, 5, 10, 15, 20, 27, 34, 41, 48, 55, 62, 69
RAA [°]	11	0.01, 15, 30, 45, 60, 80, 100, 120, 140, 160, 180
Surface reflectance [-]	4	0.0, 0.05, 0.1, 0.2
AOD at 443 nm [-]	8	0.0, 0.1, 0.4, 0.8, 1.5, 2.0, 2.8, 3.6, 5.0, 10.0
SSA at 443 nm [-]	8	1.0, 0.98, 0.96, 0.94, 0.91, 0.88, 0.85, 0.82 for HAF and Dust 1.0, 0.99, 0.98, 0.97, 0.96, 0.94, 0.92, 0.90 for NA
ALH above the surface [km]	5	0.5, 1.5, 3.0, 4.5, 6.0
Elevation [km]	3	0, 3, 6

1542

1543

**Table 2: Statistic of hourly comparison of GEMS and AERONET AOD in Figure S2S5.**

Time	N	Slope	y-intercept	R	RMSE	MBE	Q (%)	GCOS (%)
22:45	<a href="#">925801</a>	<a href="#">0.730725</a>	<a href="#">0.180177</a>	<a href="#">0.715738</a>	<a href="#">0.188181</a>	<a href="#">0.100094</a>	<a href="#">58.3860.42</a>	<a href="#">23.24.97</a>
23:45	<a href="#">19641413</a>	<a href="#">0.684728</a>	<a href="#">0.190193</a>	<a href="#">0.830752</a>	<a href="#">0.212187</a>	<a href="#">0.076115</a>	<a href="#">59.3253.93</a>	<a href="#">20.9319.89</a>
00:45	<a href="#">45932879</a>	<a href="#">0.584600</a>	<a href="#">0.217221</a>	<a href="#">0.767698</a>	<a href="#">0.224218</a>	<a href="#">0.088112</a>	<a href="#">5148.32</a>	<a href="#">16.7415.56</a>
01:45	<a href="#">56323345</a>	<a href="#">0.534490</a>	<a href="#">0.200211</a>	<a href="#">0.774715</a>	<a href="#">0.211209</a>	<a href="#">0.054063</a>	<a href="#">54.8352.68</a>	<a href="#">17.4716.95</a>
02:45	<a href="#">64003718</a>	<a href="#">0.555533</a>	<a href="#">0.183193</a>	<a href="#">0.795780</a>	<a href="#">0.221214</a>	<a href="#">0.029039</a>	<a href="#">54.5352.66</a>	<a href="#">18.5517.86</a>
03:45	<a href="#">61393504</a>	<a href="#">0.569577</a>	<a href="#">0.165171</a>	<a href="#">0.824830</a>	<a href="#">0.233238</a>	<a href="#">0.013011</a>	<a href="#">56.5453.48</a>	<a href="#">17.0416.67</a>
04:45	<a href="#">61573556</a>	<a href="#">0.593592</a>	<a href="#">0.169176</a>	<a href="#">0.822824</a>	<a href="#">0.230238</a>	<a href="#">0.000001</a>	<a href="#">55.1953.12</a>	<a href="#">18.1617.97</a>
05:45	<a href="#">56423186</a>	<a href="#">0.586518</a>	<a href="#">0.204233</a>	<a href="#">0.773725</a>	<a href="#">0.235043</a>	<a href="#">0.041043</a>	<a href="#">52.8750.00</a>	<a href="#">19.2518.33</a>
06:45	<a href="#">42612117</a>	<a href="#">0.647606</a>	<a href="#">0.218241</a>	<a href="#">0.794766</a>	<a href="#">0.233239</a>	<a href="#">0.065069</a>	<a href="#">54.8952.01</a>	<a href="#">19.4679</a>
07:45	<a href="#">25411299</a>	<a href="#">0.617632</a>	<a href="#">0.224227</a>	<a href="#">0.771754</a>	<a href="#">0.247245</a>	<a href="#">0.054063</a>	<a href="#">56.5554.89</a>	<a href="#">19.4886</a>

1544

1545

1546

1547

1548

1549

**Table 3: Comparison of GEMS and AERONET SSA for different aerosol types in Figure 9. N represents the number of data, and EE% denotes the percentage within the expected error range of  $\pm 0.03$  ( $\pm 0.05$ ).**

Aerosol Type	GEMS AOD > 0.4		GEMS AOD > 1.0	
	N	EE% $\pm 0.03$ ( $\pm 0.05$ )	N	EE% $\pm 0.03$ ( $\pm 0.05$ )
All	<a href="#">52271841</a>	<a href="#">42.76(67.2534.22(61.38))</a>	<a href="#">454174</a>	<a href="#">56.61(83.7048.85(84.48))</a>
HAF	<a href="#">1559764</a>	<a href="#">41.95(70.2431.68(62.43))</a>	<a href="#">277136</a>	<a href="#">61.01(87.7354.41(89.71))</a>
Dust	<a href="#">43771</a>	<a href="#">20.37(50.5712.68(45.07))</a>	<a href="#">8215</a>	<a href="#">39.02(73.1713.33(66.67))</a>
NA	<a href="#">1850536</a>	<a href="#">45.14(65.6232.46(56.72))</a>	<a href="#">317</a>	<a href="#">51.61(70.9742.86(57.14))</a>

1550

1551

**Table 4: Statistic of comparison of GEMS and AERONET SSA in Figure S4S6.**

Time	GEMS AOD > 0.4		GEMS AOD > 1.0	
	N	EE% $\pm 0.03$ ( $\pm 0.05$ )	N	EE% $\pm 0.03$ ( $\pm 0.05$ )
22:45	<a href="#">13749</a>	<a href="#">64.96(86.1367.35(89.80))</a>	<a href="#">2313</a>	<a href="#">52.17(86.9661.54(92.31))</a>
23:45	<a href="#">28876</a>	<a href="#">60.76(83.6864.47(82.89))</a>	<a href="#">6718</a>	<a href="#">74.63(92.5477.78(94.44))</a>
00:45	<a href="#">420100</a>	<a href="#">57.62(82.38.00(87.00))</a>	<a href="#">9321</a>	<a href="#">73.12(88.1790.48(100.00))</a>
01:45	<a href="#">454138</a>	<a href="#">56.61(79.0757.25(81.16))</a>	<a href="#">11329</a>	<a href="#">63.72(88.50.41(96.55))</a>
02:45	<a href="#">655190</a>	<a href="#">39.69(62.9031.58(56.84))</a>	<a href="#">23772</a>	<a href="#">45.99(73.0031.94(56.94))</a>
03:45	<a href="#">859391</a>	<a href="#">27.82(53.2018.67(44.76))</a>	<a href="#">339206</a>	<a href="#">25.07(57.2315.05(46.60))</a>
04:45	<a href="#">822406</a>	<a href="#">28.22(55.60).41(52.46)</a>	<a href="#">335209</a>	<a href="#">27.76(62.3923.44(58.85))</a>
05:45	<a href="#">621223</a>	<a href="#">3630.49(61.88(63.12))</a>	<a href="#">22294</a>	<a href="#">38.29(67.5728.72(65.96))</a>
06:45	<a href="#">620175</a>	<a href="#">48.23(73.2337.14(69.71))</a>	<a href="#">25583</a>	<a href="#">51.37(77.6540.96(75.90))</a>
07:45	<a href="#">35193</a>	<a href="#">60.68(79.4953.76(73.12))</a>	<a href="#">16046</a>	<a href="#">63.12(84.3854.35(76.09))</a>

1552